Cell Reports

Article

Intron retention of an adhesion GPCR generates 1TM isoforms required for 7TM-GPCR function

Graphical abstract

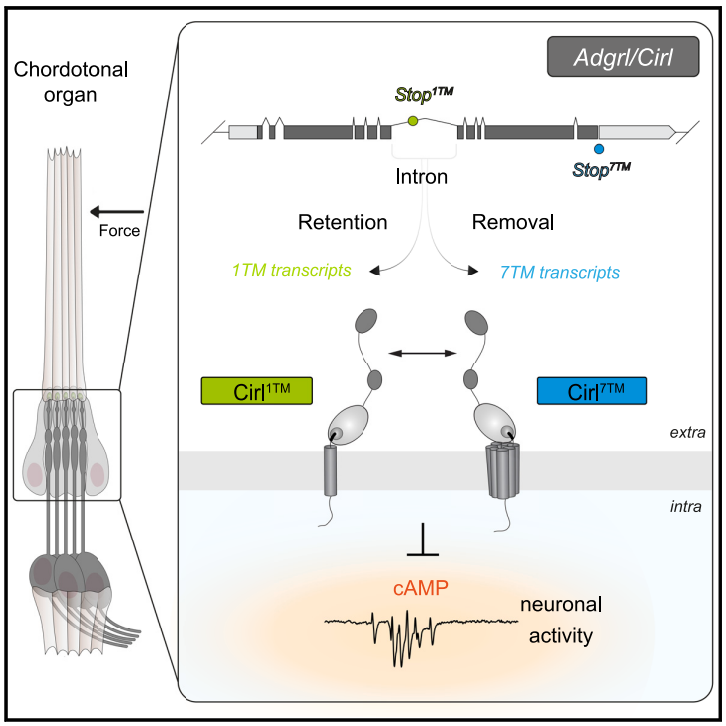

Highlights

- aGPCR *Adgrl/Cirl* is alternatively spliced, encoding atypical 1TM-containing proteins
- NTF of Cirl^{1TM} binds conventional aGPCR protein (Cirl^{7TM}) made from the same gene
- Cirl isoform interplay enables accurate mechanosensitivity of sensory neurons
- Mechanosensory precision is determined by Gα_o-dependent modulation of cAMP

Authors

Anne Bormann, Marek B. Körner, Anne-Kristin Dahse, ..., Tobias Langenhan, Dmitrij Ljaschenko, Nicole Scholz

Correspondence

dmitrij.ljaschenko@medizin.uni-leipzig.de (D.L.), scholzlab@gmail.com (N.S.)

In brief

Bormann et al. investigated the adhesion GPCR ADGRL/Cirl in living *Drosophila*. Their research introduces a concept where structurally unconventional non-GPCR isoforms act in conjunction with conventional GPCRs originating from the same gene locus. This interaction determines how sensory neurons respond to mechanical stimulation.

Bormann et al., 2025, Cell Reports *44*, 115078
January 28, 2025 © 2024 The Author(s). Published by Elsevier Inc.
https://doi.org/10.1016/j.celrep.2024.115078

CellPress

Cell Reports

CellPress
OPEN ACCESS

Article

Intron retention of an adhesion GPCR generates 1TM isoforms required for 7TM-GPCR function

Anne Bormann,[1,9] Marek B. Körner,[1,2,9] Anne-Kristin Dahse,[1,9] Marie S. Gläser,[1] Johanna Irmer,[1] Vera Lede,[3] Judith Alenfelder,[4] Joris Lehmann,[1,5] Daniella C.N. Hall,[1,6] Michael Thane,[7] Michael Schleyer,[7,8] Evi Kostenis,[4] Torsten Schöneberg,[3] Marina Bigl,[1] Tobias Langenhan,[1] Dmitrij Ljaschenko,[1,*] and Nicole Scholz[1,10,*]

[1]Rudolf Schönheimer Institute of Biochemistry, Division of General Biochemistry, Medical Faculty, Leipzig University, 04103 Leipzig, Germany
[2]Institute of Human Genetics, University of Leipzig Medical Center, 04103 Leipzig, Germany
[3]Rudolf Schönheimer Institute of Biochemistry, Division of Molecular Biochemistry, Medical Faculty, Leipzig University, 04103 Leipzig, Germany
[4]Molecular, Cellular and Pharmacobiology Section, Institute for Pharmaceutical Biology, University of Bonn, 53115 Bonn, Germany
[5]Institute of Biology/Zoology, Department of Animal Physiology, Martin Luther University Halle-Wittenberg, 06120 Halle, Germany
[6]Institute of Pharmacy, Martin Luther University Halle-Wittenberg, 06120 Halle, Germany
[7]Department of Genetics Learning and Memory, Leibniz Institute for Neurobiology, 39118 Magdeburg, Germany
[8]Institute for the Advancement of Higher Education, Hokkaido University, Sapporo 060-08080, Japan
[9]These authors contributed equally
[10]Lead contact
*Correspondence: dmitrij.ljaschenko@medizin.uni-leipzig.de (D.L.), scholzlab@gmail.com (N.S.)
https://doi.org/10.1016/j.celrep.2024.115078

SUMMARY

Adhesion G protein-coupled receptors (aGPCRs) are expressed in all organs and are involved in various mechanobiological processes. They are heavily alternatively spliced, forecasting an extraordinary molecular structural diversity. Here, we uncovered the existence of unconventional single-transmembrane (1TM)-containing ADGRL/Cirl proteins devoid of the conventional GPCR layout (i.e., the 7TM signaling unit) in *Drosophila*. These 1TM proteins are made as a result of intron retention and provide an N-terminal fragment that acts as an interactor to allow $G\alpha_o$-dependent signaling through conventional 7TM-containing Cirl isoforms encoded by the same gene. This molecular mechanism determines sensory precision of neurons in response to mechanical stimulation *in vivo*. This action mode of aGPCR provides a promising entry point for experimental and therapeutic approaches to intervene in aGPCR signaling and implicates alternative splicing as a physiological strategy to express a given aGPCR together with its molecular interactor.

INTRODUCTION

G protein-coupled receptors (GPCRs) assume roles in numerous fundamental biological processes and are some of the most important pharmacological targets to treat diseases.[1] The linchpin shared by all GPCRs (class A, B, and C receptors) is the transmembrane domain with seven transmembrane-spanning α helices (7TM), basic for the conversion of extracellular signals into intracellular biochemical responses. The vast majority of GPCRs sense chemical signals. However, over the last decade, adhesion GPCRs (aGPCRs/ADGRs, class B), the second largest GPCR class in humans,[2] have been identified as receptors regulating mechanobiological processes.[3–11]

aGPCRs are expressed in every organ, and several members are enriched in neural tissues,[12] whose development, morphology, and function are known to be shaped by mechanosensing.[13–15] However, a mechanistic understanding of how aGPCRs contribute to these processes remains elusive.

aGPCR are encoded by large genomic loci characterized by a complex exon-intron architecture allowing alternative splicing. This, together with multiple promoters and/or transcriptional readthrough, has been shown to result in an average of 19 and 24 transcript variants from a given mouse and human aGPCR gene, respectively.[16,17] Like other GPCRs, aGPCRs are comprised of an extracellular region (ECR), a 7TM domain, and an intracellular region (ICR), which includes intracellular loops (ICL) and the C-tail. However, the ECRs of aGPCRs usually contain several extracellular domains including a GPCR autoproteolysis-inducing (GAIN) domain,[18] which promotes their bipartition into large extracellular N-terminal fragments (NTFs) and non-covalently attached C-terminal fragments (CTFs), which encompass the 7TM and C-tail. Bioinformatic analysis of the transcript repertoire of aGPCR in the mouse suggests variable structural layouts of putative receptor variants (hereafter referred to as isoforms) derived from alternative splicing and intragenic promoters affecting virtually every part of the aGPCR protein.[17] To date, in-depth analyses of only a few aGPCR isoforms have been done *in vivo*.[19–21] A recent study of LPHN3/ADGRL3 in the hippocampus has impressively demonstrated the importance of alternative splicing for L3 signaling and, ultimately, synapse formation.[20] The individual aGPCR isoforms studied thus far are characterized by structural changes affecting the NTF or CTF.[19–21]

This is an open access article under the CC BY-NC-ND license (http://creativecommons.org/licenses/by-nc-nd/4.0/).

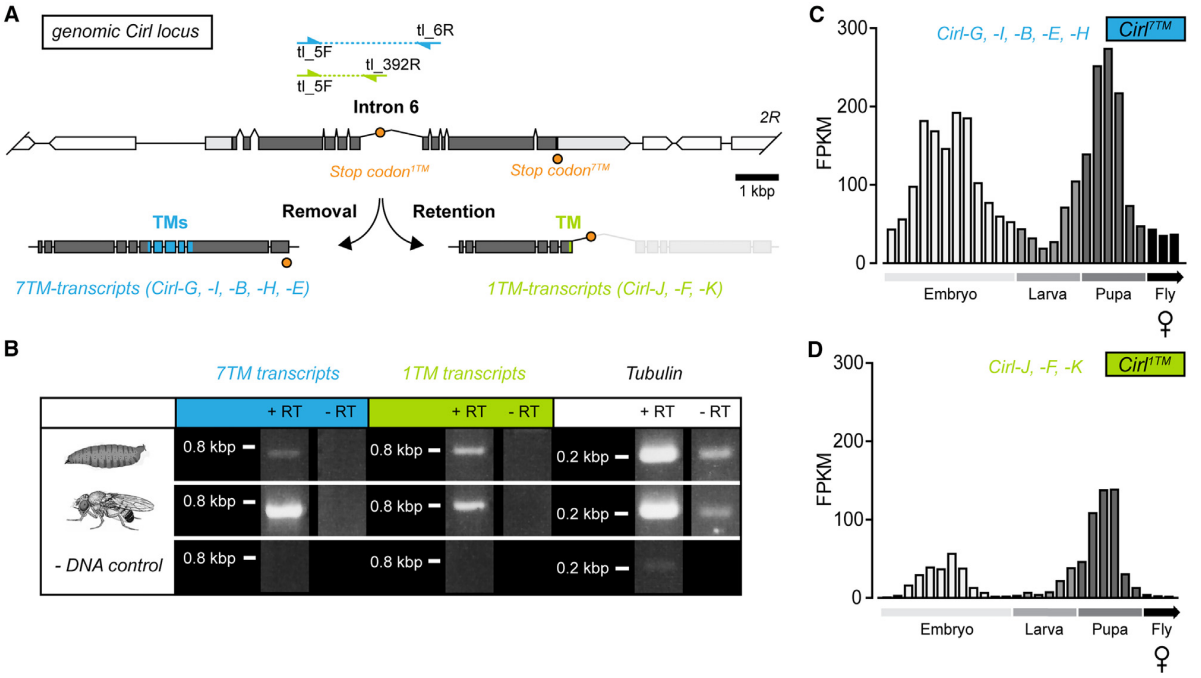

Figure 1. Intron retention produces *Cirl* transcripts encoding proteins with a single TM and alternative ICR

(A) Schematic of the *Cirl* gene locus. Removal of intron 6 gives rise to five $Cirl^{7TM}$ transcripts (blue). Retention of intron 6 generates three $Cirl^{1TM}$ transcripts (green). Layout of the corresponding proteins is shown in Figures S1A and S1B.

(B) Validation of $Cirl^{1TM}$ transcript in *Drosophila*. RT-PCR products amplified from larval and adult cDNAs for $Cirl^{7TM}$ (blue, 0.7 kbp) and $Cirl^{1TM}$ transcripts (green, 0.8 kbp). Tubulin, loading and quality control of cDNA and RT-PCR; no DNA, specificity control.

(C and D) Sum of FPKM (cumulative fragments per kilobase million) values of $Cirl^{7TM}$ (C) and $Cirl^{1TM}$ (D) mRNAs at several developmental time points. $Cirl^{7TM}$ and $Cirl^{1TM}$ have a similar ontogenetic expression profile, but $Cirl^{7TM}$ transcript quantity was higher than that of $Cirl^{1TM}$. Embryo (white), 12 time points equally distributed between 0 and 24 h; larval stages (light gray) L1, L2, and L3 (split across 6 time points) in days; pupa (dark gray): 6 time points across 4 days; female flies (black): 1, 5, and 30 days old. Analysis was done using previously published data[23] (Database: SRP001065). For individual transcript quantities, see Figures S1C and S1D.

See also Table S1.

In the present study, we investigated a prototype aGPCR, the ADGRL/Latrophilin homolog *Cirl* (Ca^{2+}-independent receptor of latrotoxin) in *Drosophila* and uncovered the expression of unconventional non-GPCR isoforms that lack the 7TM signaling unit and only contain a single transmembrane helix ($Cirl^{1TM}$). Transcripts encoding such putative non-GPCR isoforms are also predicted for several mammalian aGPCRs;[16,17] however, whether they are translated and whether they are functional is not known. $Cirl^{1TM}$ appears to be the result of intron retention, the most enigmatic among the alternative splicing mechanisms.[22] RNA sequencing and bioinformatics revealed that $Cirl^{1TM}$ transcripts are co-expressed with $Cirl^{7TM}$ transcripts, which encode conventional 7TM-containing aGPCR isoforms ($Cirl^{7TM}$), throughout development. The resulting proteins locate, at least partly, to similar subcellular sites in mechanosensory neurons. Moreover, co-immunoprecipitation (coIP) experiments suggest a direct interaction between $Cirl^{1TM}$ and $Cirl^{7TM}$ at the level of the NTF. Consistent with the ontogenetic and subcellular expression profile as well as the physical interaction, we show that $Cirl^{1TM}$ and $Cirl^{7TM}$ are equally required *in vivo* to determine the mechanosensory capacity of sensory neurons. Our functional analyses *in vivo* show that the underlying mechanism depends on $Cirl^{7TM}$, the $Cirl^{1TM}$-ECR (includes NTF), and on $G\alpha_o$-dependent signaling through $Cirl^{7TM}$. In sum, these findings suggest a model where intron retention generates non-GPCR $Cirl^{1TM}$ proteins as an NTF source required for $G\alpha_o$-dependent signaling through GPCR-$Cirl^{7TM}$ to determine the responsiveness of sensory neurons toward mechanical stimulation. This action mode may be an important avenue to modulate aGPCR signaling and establishes a causal link between alternative splicing of aGPCR and neuronal mechanosensation.

RESULTS

Intron retention produces *Cirl* transcripts encoding proteins with a single TM domain and alternative ICR

In *Drosophila*, Cirl/Latrophilin/ADGRL is encoded by a single gene.[10] Alternative splice events of *Cirl* pre-mRNA produce eight different transcripts (flybase.org) putatively encoding six individual proteins (Figures 1A, S1A, and S1B). The majority of transcripts encode conventional GPCRs that contain a 7TM domain, which allows G protein engagement, β-arrestin binding, and

canonical intracellular signaling (Cirl^{7TM} types = *Cirl-G*, *-I*, *-B*, *-E*, and *-H*; Figures 1A, S1A, and S1C). However, a substantial fraction of transcripts encodes proteins containing an ECR that is anchored within the plasma membrane by only a single TM helix (Cirl^{1TM} types = *Cirl-J*, *-F*, and *-K*; Figures 1A, S1B, and S1D). These *Cirl^{1TM}* transcripts likely arise through intron retention, where a specific splice donor is ignored, and intron 6 is retained in the mRNA. The resulting transcripts are either degraded or translated. In the latter case, translation would continue until an intronic in-frame stop codon is reached, producing 207 alternative amino acid residues of the putative Cirl^{1TM} isoforms (Figure 1A).

To confirm the presence of *Cirl^{1TM}* transcripts, we performed RT-PCR analyses on cDNA libraries generated from wild-type (*w^{1118}*) adult and larval *Drosophila* using *Cirl^{1TM}*- and *Cirl^{7TM}*-specific primer sets (Figure 1A). We were able to amplify *Cirl^{1TM}*- and *Cirl^{7TM}*-specific DNA fragments (Figure 1B), implying expression of both in larvae and adult flies. To rule out the possibility that *Cirl^{1TM}* transcripts destined for degradation served as PCR templates, and to investigate whether *Cirl^{1TM}* and *Cirl^{7TM}* are consistently co-expressed, we quantified the amount of each *Cirl* transcript generated at consecutive time points during embryonic, larval, pupal, and adult development using a previously generated RNA sequencing dataset[23] (Figures S1C and S1D; Data S1). *Cirl^{7TM}* and *Cirl^{1TM}* transcripts show similar ontogenetic expression profiles with peak abundance during embryonic and pupal stages (Figures 1C, 1D, S1C, and S1D). *Cirl^{1TM}* and *Cirl^{7TM}* account for ~22.5% and ~77.5% of total *Cirl* transcript produced, respectively (Figure S1E). These data confirm the expression of *Cirl^{1TM}* transcripts and suggest that *Cirl^{1TM}* and *Cirl^{7TM}* transcript expression is co-regulated. This implies the need for both transcript types during development and particularly in embryonic and pupal stages, which are signified by morphogenetic movements that elicit mechanical forces. Our findings are in agreement with the recently uncovered role of Cirl in embryonic and late larval development,[11,24] adding a mechanistic detail still to be explored.

Cirl^{1TM} protein is expressed *in vivo*

Currently, there are no antibodies available to detect Cirl protein. Hence, to ascertain whether *Cirl^{1TM}* transcripts are translated into Cirl^{1TM} proteins *in vivo*, we used the previously generated *Cirl^{KO}-attP* allele[10] to reinstate the genomic *Cirl* locus including sequences that encode different tags (*mRFP*, *2xV5*, and *3xFLAG*; Figure 2A). This strategy allows isoform-specific detection through matching commercially available antibodies. The resulting allele is referred to as *Cirl$^{3x\text{-}tagged}$* (Figure 2A). The Cirl^{1TM} proteins made from this locus contain an monomeric Red Fluorescent Protein (mRFP) within the NTF[25] and a 2xV5 tag at the far C-terminus (Figure 2B). Cirl^{7TM} proteins made from the same locus also carry an mRFP within the NTF[25] as well as a 3xFLAG tag in the third ICL (ICL3; Figure 2B). Thus, an antibody directed against mRFP detects the entire Cirl isoform repertoire,[25] whereas anti-V5 and anti-FLAG antibodies recognize Cirl^{1TM} and Cirl^{7TM}, respectively. Importantly, *Cirl$^{3x\text{-}tagged}$* and all other *Cirl* alleles employed in this study were generated using this knockin strategy (i.e., insertion of genomic sequences) and are thus expressed under transcriptional control of the native *Cirl* promoter and regulatory elements. Our RNA sequencing data suggested the highest *Cirl* expression in pupae (Figures 1C and 1D). Therefore, we first immunoprecipitated Cirl proteins from extracts of *Cirl$^{3x\text{-}tagged}$* pupae using anti-RFP functionalized magnetic beads (Figure 2C). Using anti-V5, we specifically detected the CTF of Cirl^{1TM} (Figure 2D). Unfortunately, the specific detection of Cirl^{7TM} failed due to unspecific binding of the anti-FLAG antibody.

Autoproteolytic processing at the GAIN domain presents one of the hallmark features of aGPCR and underlies their bipartite NTF/CTF structure. Autoproteolysis of Cirl can be averted by mutating the GPCR proteolysis site (GPS).[25] To further substantiate the existence of Cirl^{1TM} proteins, we generated a cleavage-deficient version of *Cirl$^{3x\text{-}tagged}$* via an H>A mutation within the GPS (*Cirl$^{3x\text{-}tagged\text{-}GPS/H>A}$*).[25] As expected, western blot analysis revealed full-length (FL) Cirl^{1TM} at ~170 kDa (Figure 2D). We detected two additional bands of unknown identity: an ~140 kDa fragment, which matches the molecular weight of non-glycosylated FL Cirl^{1TM}, and an ~70 kDa fragment, which most likely results from additional cleavage of the NTF, not uncommon for aGPCR[26] (Figure 2D). Consistent with the latter finding, in head extracts, we find an ~75 kDa N-terminal band using anti-RFP antibody (Figure 2E, white circle), which could represent the counterpiece to the ~70 kDa C-terminal band (Figure 2D, white arrowhead). More importantly, this anti-RFP staining also shows protein bands whose molecular masses correspond to FL Cirl^{1TM} and FL Cirl^{7TM} (Figure 2E). Quantification of corresponding signals showed that Cirl^{1TM} accounts for ~35% and Cirl^{7TM} for ~65% of the entire Cirl protein repertoire (Figure 2F). In sum, these results confirm that *Cirl^{1TM}* transcripts are translated to produce Cirl^{1TM} proteins *in vivo*.

Cirl^{1TM} protein localizes to mechanosensory neurons

Previously, we reported Cirl's role in larval mechanosensitive neurons of the lateral pentascolopidial (lch5) organ.[10,25] The lch5 organ consists of a defined number of support cells encasing five monociliated sensory neurons (Figures 3F and 3G). The organ is suspended between the muscle and cuticle to sense sound, touch, and proprioceptive stimuli.[10,27] Because of its well-understood anatomy, manageable cell numbers, and experimental accessibility, we are utilizing this system here to decipher individual contributions of the different Cirl isoform types and especially those of Cirl^{1TM} proteins. The *Cirl^{KO}* allele used in previous studies removes both the Cirl^{7TM} and Cirl^{1TM} isoforms (1TM type, 2 isoforms; 7TM type, 4 isoforms).[10,11,25] To gain genetic control over Cirl isoform expression, we engineered two *Cirl* alleles for mutually exclusive expression of either Cirl^{1TM} or Cirl^{7TM} gene products under endogenous transcriptional control (Figures 3A–3D). Sole expression of Cirl^{7TM} was achieved by removing the intron (intron 6 of isoform *I*, corresponding to intron 5 of *E*, *B/H*, and *G*) that could otherwise encode the C-tail of Cirl^{1TM} (Figures 3A and 3B). Sole expression of Cirl^{1TM} was achieved by a silent mutation of the splice donor (*GT* → *CT*) at the exon 6/intron 6 boundary and removal of the *Cirl^{7TM}*-specific gene region that follows intron 6 (Figures 3C and 3D). The resulting Cirl^{7TM} and Cirl^{1TM} proteins contained 2xV5 in the ICL3 and at the C terminus, respectively, for immunodetection purposes (Cirl^{7TM}::2xV5 and Cirl^{1TM}::2xV5; Figures 3B and 3D). To validate our genetic strategy, we conducted western

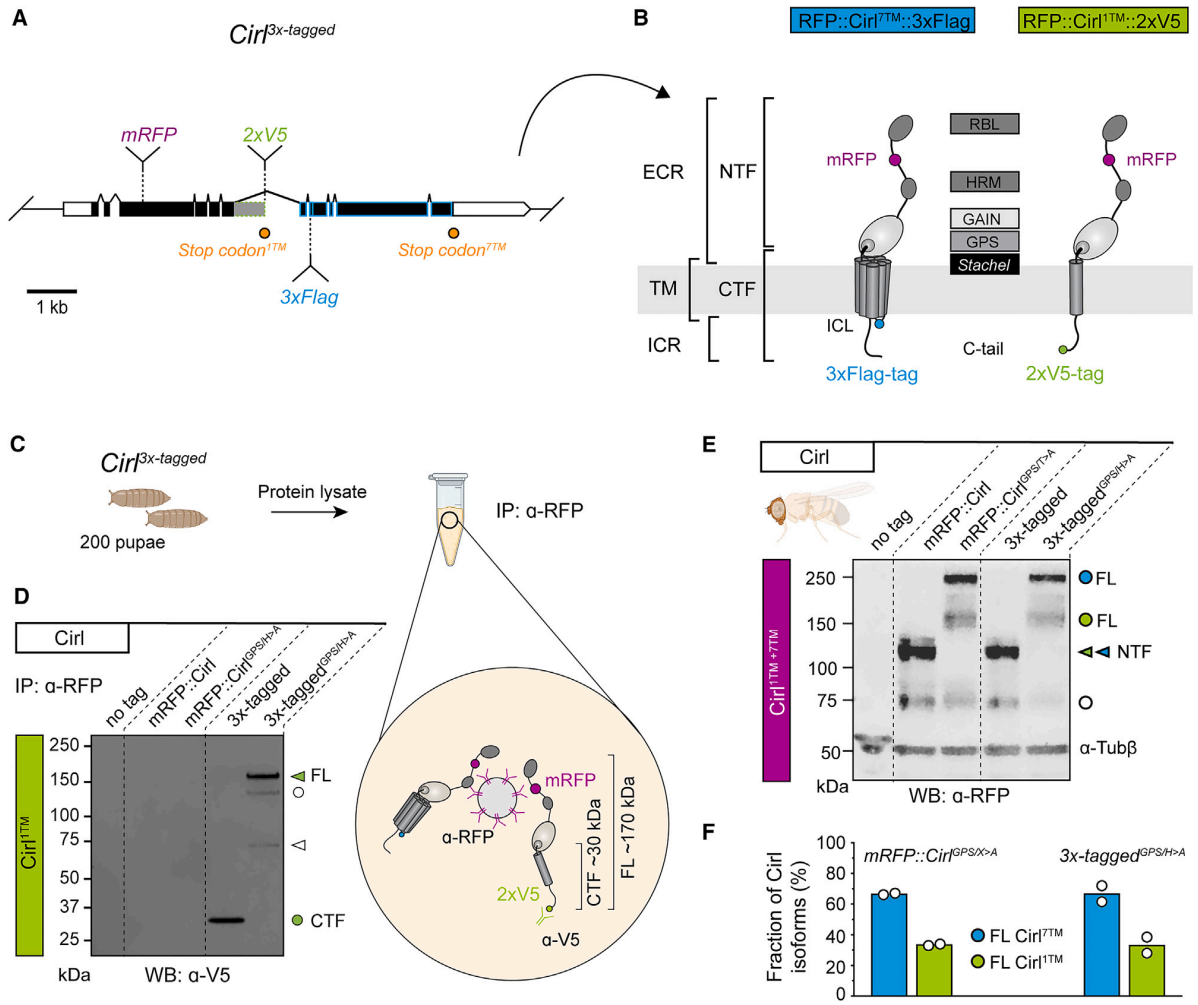

Figure 2. Cirl^{1TM} protein is expressed *in vivo*

(A) Schematic of the *Cirl*$^{3x\text{-}tagged}$ locus. Insertion sites of mRFP (in magenta) and 2xV5 (in green) and 3xFLAG (in blue) sequences are indicated.

(B) Layout of *Cirl*$^{3x\text{-}tagged}$-encoded proteins. mRFP is located between the rhamnose binding lectin (RBL) domain and hormone receptor-binding motif (HRM) domain of Cirl^{7TM} and Cirl^{1TM} proteins,[25] the 2xV5-tag at the C-terminal end of Cirl^{1TM}, and 3xFlag in the ICL3 of Cirl^{7TM}. ECR, extracellular region; TM, transmembrane; ICR, intracellular region (C-tail and ICL1-3); NTF, N-terminal fragment; CTF, C-terminal fragment.

(C) Schematic of the experimental configuration. Shown is protein extraction from wild-type and cleavage-deficient *Cirl*$^{3x\text{-}tagged}$ pupae followed by IP using anti-RFP functionalized magnetic beads. Both Cirl isoform types can be immobilized via the N-terminal mRFP tag. Anti-V5 exclusively detects immobilized Cirl^{1TM} via its C-terminal 2xV5 tag.

(D) Western Blot of the IP experiment depicted in (C). Anti-V5 staining reveals CTF of GPS cleavage-competent Cirl^{1TM}::2xV5 (~30 kDa, green circle). FL Cirl^{1TM}::2xV5 (~170 kDa, green arrowhead) was detected when GPS cleavage was disabled (H>A). 140 kDa (white circle) and 70 kDa (white arrowhead) are bands of unknown identity. Specificity control: *Cirl*^{Recsue}; i.e., no tag. See also Figure S4A.

(E) Western blot analysis of fly head homogenates confirms Cirl^{7TM} and Cirl^{1TM} expression. Anti-RFP recognized the NTFs of RFP::Cirl^{1TM} and RFP::Cirl^{7TM} (~120 kDa, green and blue arrowheads) in samples from *mRFP::Cirl* and *Cirl*$^{3x\text{-}tagged}$ animals. FL Cirl^{1TM} (~165 kDa, green circle) and FL Cirl^{7TM} (~260 kDa, blue circle) were detected in samples derived from *RFP::Cirl*$^{GPS/T>A}$[25] and *Cirl*$^{3x\text{-}tagged\text{-}GPS/H>A}$ mutants, which express GPS cleavage-deficient proteins. ~75 kDa (white circle), band of unknown identity. Specificity control: *Cirl*^{Recsue}; i.e., no tag. Tubulin (α-Tubβ), loading control.

(F) Quantification of anti-RFP signals derived from cleavage-deficient Cirl proteins of *mRFP::Cirl*$^{GPS/T>A}$ and *Cirl*$^{3x\text{-}tagged\text{-}GPS/H>A}$ animals shown in (E). This experiment was repeated with similar results (N = 2, data presented as mean). Note that, in the second experiment, *mRFP::Cirl*$^{GPS/H>A}$ was used instead of *mRFP::Cirl*$^{GPS/T>A}$ mutants. Cirl^{1TM} accounts for approximately 35% of all Cirl proteins.

CellPress
OPEN ACCESS

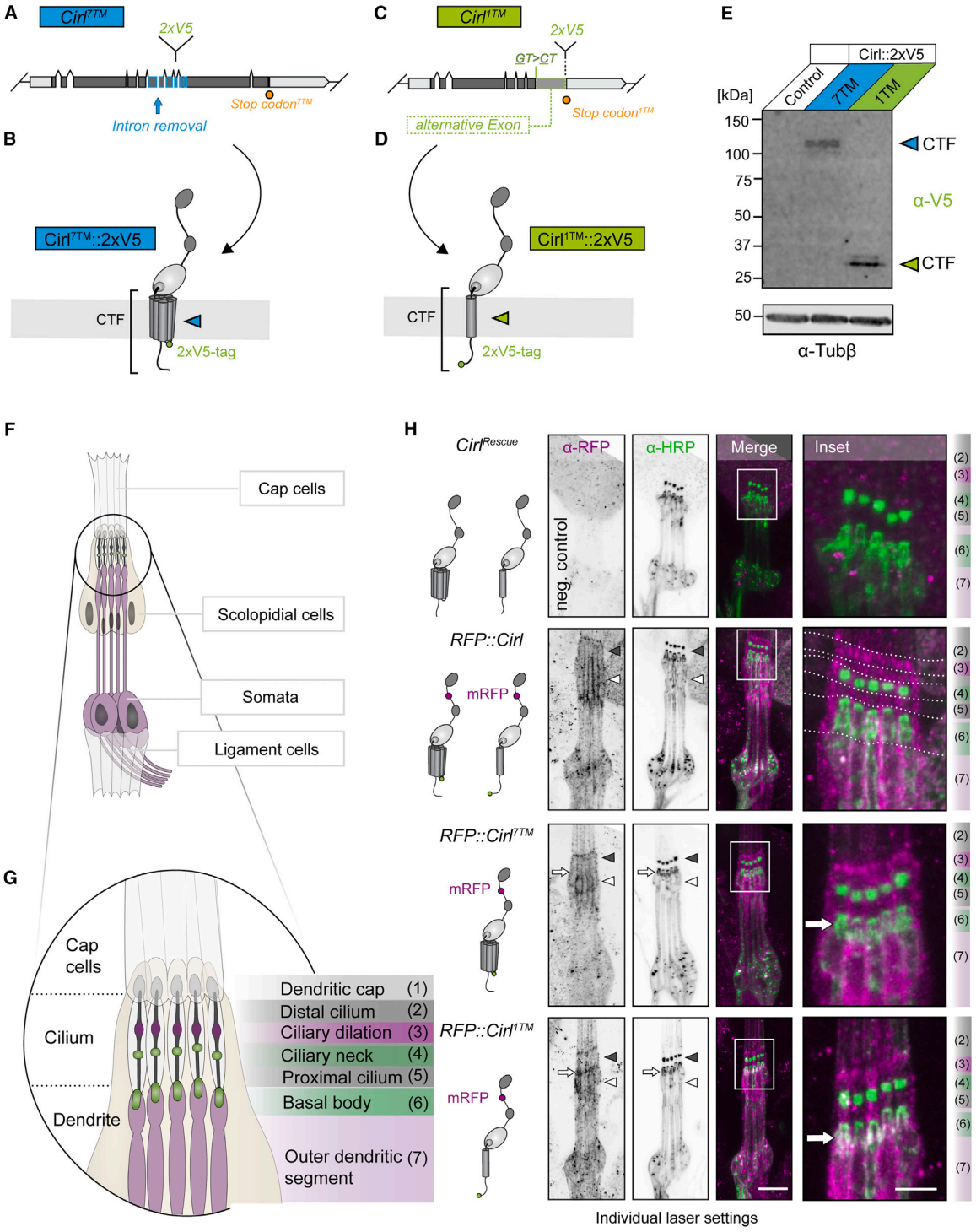

Figure 3. Cirl^{1TM} protein localizes to mechanosensory neurons

(A) Illustration of the genetic manipulation of the *Cirl* locus to exclusively express Cirl^{7TM} isoforms. Intron 6, which encodes the C-terminus of Cirl^{1TM}, was removed. 2xV5 sequences were introduced at ICL3 for protein detection.

(legend continued on next page)

blot analyses (Figure 3E) and specifically detected the CTFs of Cirl^{7TM} (~110 kDa) or Cirl^{1TM} (~30 kDa) using an anti-V5 antibody (Figure 3E). Unfortunately, anti-V5 immunofluorescence detection via confocal imaging of Cirl^{1TM}::2xV5 in lch5 organs failed due to high background signal (data not shown). To bypass this technical issue and to locate Cirl^{1TM} in lch5 organs, we generated another set of *Cirl^{1TM}* and *Cirl^{7TM}* alleles containing an additional N-terminal mRFP (RFP::Cirl^{1TM}::2xV5 and RFP::Cirl^{7TM}::2xV5; Figure 3H).[25] Anti-RFP immunolabeling and microscopy of larval lch5 organs revealed specific signals of both Cirl^{1TM} and Cirl^{7TM} at the level of the ciliary and outer dendritic segments as well as at the ciliary dilation of mechanosensory neurons (Figure 3H). Anti-horseradish peroxidase (HRP) was used to visualize neuronal lch5 plasma membranes. *Cirl^{Rescue}* express unaltered, untagged proteins from the *Cirl* locus and served as a negative control. In the outer dendritic segment, particularly around the basal body, we detected mostly Cirl^{1TM} protein (Figure 3H). Thus, mechanosensory lch5 organs express Cirl^{1TM} proteins in addition to Cirl^{7TM} receptors, and both can occupy similar subcellular compartments.

Cirl^{1TM} and Cirl^{7TM} proteins are co-required for neuronal discrimination between different mechanical input intensities

To pinpoint the functional relevance of different Cirl isoform types, we performed electrophysiological recordings from mechanostimulated lch5 neurons. Previously, measurements from lch5 neurons showed that *Cirl^{KO}* larvae discriminate less robustly between different vibrational stimulation frequencies than controls (*Cirl^{Rescue}*).[10,25] However, the previously used direct vibration stimulation of the lch5 offered no control over the stimulus amplitude.[10,25] To increase stimulation precision and to more adequately emulate proprioceptive stretch-induced lch5 activity, we attached a miniature hook to a piezo element, which was moved defined distances between 0.03 and 3 μm perpendicular to the lch5 organ (Figures 4A and 4B). This way, the organ is stretched to trigger action currents (ACurr; Figures 4B and 4C) with remarkably low variability, thus increasing resolution.

The lch5 neurons of *Cirl^{Rescue}* larvae responded to 0.03 μm pulls with a mean ACurr frequency of 140 Hz. The frequency increased with higher stimulus intensities to 325 Hz at a 3 μm pull ($\Delta_{0.03–3\mu m}$ = 185 Hz; Figure 4G; Table S3), which shows that lch5 neurons can differentiate between these pull lengths; i.e., mechanical stimulation intensities. In contrast, lch5 neurons of *Cirl^{KO}* were significantly less capable of discriminating between different pull lengths ($\Delta_{0.03–3\mu m}$ = 26 Hz; Figure 4G; Table S3). Hence, in *Cirl^{KO}*, the lch5 output signal relayed to the central nervous system remains virtually unaltered, although the actual stimulation intensity had drastically increased. This finding is consistent with the discrimination deficit between different vibration frequencies in *Cirl^{KO}*.[10]

As Cirl is already known to be involved in sound detection through lch5 mechanosensory organs,[10] we wondered about the involvement of Cirl^{1TM}. Therefore, we measured Ca^{2+} signals in single neurons elicited by sound using the genetically encoded indicator jGCaMP7f[28] (Figures S2A and S2B). Interestingly, lch5 neurons in *Cirl^{Rescue}* animals responded differently to the same sound, and the largest response was documented in the most ventral neuron (neuron 1; Figure S2C; Table S5). This finding suggests that individual lch5 neurons are tuned differentially. Judging from Ca^{2+} signals from neuron 1, loss of either Cirl^{1TM} or Cirl^{7TM} seems to have a similar effect as losing both (Figure S2E). Note that, although a sizable difference between *Cirl^{Rescue}* and *Cirl^{KO}* was recorded, the high variability of single-cell Ca^{2+} signals in *Cirl^{KO}* hindered the detection of a robust signal difference when compared to *Cirl^{Rescue}* (Figure S2D; Table S6). This variability prevents conclusions about how Cirl affects sound-evoked Ca^{2+} signals in individual lch5 neurons.

A much smaller variability was observed in ACurr generation when we recorded stretch-induced compound electrical signals from lch5 neurons (Figures 4A and 4G–4I). Therefore, we returned to our electrophysiological readout, which uncovered that responses from lch5 neurons of *Cirl^{7TM}* or *Cirl^{1TM}* phenocopied those of *Cirl^{KO}* animals (Figures 4D, 4E, 4G, and 4H; Tables S3 and S4). This finding suggests that regular mechanosensing depends on both isoform types and, the absence of additive effects in *Cirl^{KO}*, points toward a common signaling pathway. Importantly, the small biochemical tags that we inserted at the C-terminus of Cirl^{1TM} (Figure S3; Tables S3 and S4) or within ICL3 of Cirl^{7TM} had no impact on protein function.[25] To further substantiate that both isoform types are required to rescue the mechanosensory deficit, we measured the ACurr frequencies from *trans*-heterozygous *Cirl^{1TM}/Cirl^{7TM}* (*Cirl$^{1TM+7TM}$*) animals with the reconstituted (i.e., entire natural Cirl) isoform repertoire. Electrophysiological lch5 responses to mechanical stimulation in these animals ($\Delta_{0.03–3\mu m}$ = 106 Hz; Figures 4F and 4I; Tables S3 and S4) were comparable to *Cirl^{Rescue}* despite the fact that they contained only a single allele copy of *Cirl^{1TM}* or *Cirl^{7TM}*. This indicates that it is not the absolute amount of Cirl expressed that is important, but rather the

(B) Illustration of 2xV5-tagged Cirl^{7TM} protein expressed from the *Cirl* locus depicted in (A).
(C) Illustration of the genetic manipulation of the *Cirl* locus to exclusively express Cirl^{1TM} isoforms. The splice donor at the exon 6-intron 6 boundary was mutated (*GT* > *CT*), and 7TM-coding downstream sequences were deleted.
(D) Illustration of 2xV5-tagged Cirl^{1TM} protein expressed from the *Cirl* locus depicted in (C).
(E) Western blot analysis of head lysates from *Cirl^{7TM}* (blue, expressing only Cirl^{7TM}::2xV5) or *Cirl^{1TM}* (green, expressing only Cirl^{1TM}::2xV5) uncovered the mutually exclusive presence of CTFs derived either from Cirl^{7TM} (~110 kDa) or Cirl^{1TM} (~30 kDa). Control, *Cirl^{Rescue}* expressing untagged receptor. This experiment was repeated twice (N = 2) with similar results. Tubulin (anti-Tubβ), loading control.
(F and G) Schematic of the larval lch5 organ containing five bipolar sensory neurons. Anatomical features are numbered (1)–(7).
(H) Subcellular localization of Cirl isoform types in the lch5 organ (anti-RFP and anti-HRP channels are shown in black; images are intensity inverted). Aside from an N-terminal mRFP, Cirl^{7TM} contains a tandem V5 tag in the ICL3 (RFP::Cirl^{7TM}::2xV5), and Cirl^{1TM} contains a tandem V5 tag at the C-terminus (RFP::Cirl^{1TM}::2xV5). Anti-HRP counterstaining labels the neuronal membrane and is used to outline the lch5 neurons. Maximum intensity z projections of confocal images show RFP::Cirl^{7TM} and RFP::Cirl^{1TM} at similar subcellular regions. Negative control, *Cirl^{Rescue}* expressing untagged receptor (top row). Numbers (2)–(7) correspond to anatomical features in (G). The experiment was done in eight individual animals with similar results. Scale bars: 10 μm; inset, 5 μm.

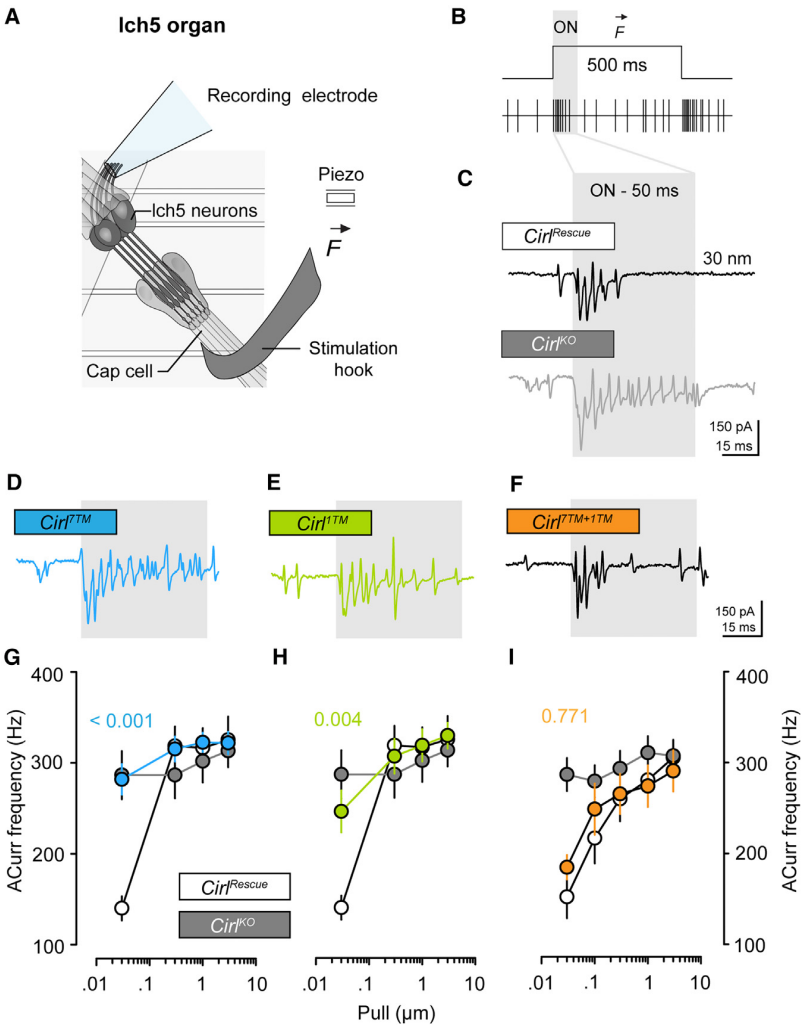

Figure 4. Cirl^{1TM} and Cirl^{7TM} proteins are co-required for neuronal discrimination between different mechanical input intensities

(A) Configuration of ACurr recordings from larval lch5 organs.

(B) Experimental protocol. Pull lengths (0.03, 0.1, 0.3, 1, and 3 μm) were applied for 500 ms. Differential reactions of the lch5 neurons as an increase of ACurr frequency after applying and releasing the pull are shown schematically. F, force.

(C) Representative ACurr traces. ACurr in the first 50 ms (gray box) after mechanostimulation onset were quantified to calculate the ACurr frequency.

(D–F) Sample ACurr traces in response to a 30 nm pull length. Gray shade, quantification period of (G)–(I).

(G–I) Quantification of ACurr frequencies in lch5 neurons at different pull lengths. Data are displayed as mean ± SEM (N = 10). The p values denote statistical difference between *Cirl^{Rescue}* and Cirl mutants at 30 nm pull length.

See also Figure S3 and Tables S3 and S4.

ratio of 1TM to 7TM proteins. Importantly, this experiment shows that the mechanosensation deficit is not an unintended consequence of the genetic engineering of the *Cirl* alleles and that the resulting Cirl^{7TM} receptor and the Cirl^{1TM} protein are fully functional. Collectively, this shows that Cirl^{7TM} (GPCR-like) isoforms require Cirl^{1TM} (non-GPCR) isoforms to tell different mechanical input intensities apart and thereby enable mechanosensation accuracy.

The NTF of Cirl^{1TM} suffices to bind Cirl^{7TM}

Our findings collectively suggest that Cirl^{1TM} and Cirl^{7TM} are co-required to modulate the neuro-mechanical response of lch5 neurons. Next, we asked whether Cirl^{1TM} and Cirl^{7TM} functions merely intersect or whether Cirl isoforms assemble signaling complexes to shape mechanosensation. To test for a direct interaction between Cirl^{1TM} and Cirl^{7TM}, we heterologously overexpressed Cirl^{7TM} (isoform E)[25] and Cirl^{1TM} (isoform F/K) in HEK293T cells and performed coIP from cell lysates (Figure 5).

First, we used hemagglutinin (HA):: Cirl^{7TM}-E as bait to capture Cirl^{1TM}-F/K::6xV5 protein (Figure 5A). Western blot analyses showed an enrichment of Cirl^{1TM}-F/K's CTF (~40 kDa) when co-expressed with HA::Cirl^{7TM}-E (Figures 5B and 5C). Quantification of these blots revealed a 9-fold increase in Cirl^{1TM}-CTF signal intensity (Figure 5D; Table S9). Importantly, when co-expressed with P2Y12 (specificity control, ~40 kDa) Cirl^{1TM} signal intensity was not increased above the background signal (Figures 5B and 5D). The blots of the corresponding input samples are shown in Figure S4B. Note that a cleavage-deficient version of Cirl^{7TM} (HA::Cirl$^{7TM\text{-}GPS/T>A}$-E, ~230 kDa; Figure 5C) was also able to capture FL Cirl$^{1TM\text{-}GPS/T>A}$-F/K::6xV5 (~130 kDa; Figure 5B), elevating its signal intensity 6-fold over that of solitarily expressed Cirl$^{1TM\text{-}GPS/T>A}$-F/K::6xV5 (Figure 5D, Table S10). The detected NTF and FL bands were often heavier than expected, which we found to be due to glycosylation, as the weight difference was abolished when samples were deglycosylated (data not shown).

Second, in an inverse experimental setup, we used HA::Cirl^{1TM}-F/K as bait to capture Cirl^{7TM}-E::6xV5 (Figure 5E). Reassuringly, we also found specific Cirl^{7TM}-Cirl^{1TM} assembly. We measured a 9-fold increase in Cirl^{7TM} signal (CTF, ~130 kDa) when Cirl^{1TM} was present. Similarly, a 7-fold increase was detected using cleavage-deficient protein variants of the same proteins (HA::Cirl$^{7TM\text{-}GPS/T>A}$-E, ~220 kDa; Figures 5F and 5G; Tables S11 and S12). The blots of the corresponding input samples are shown in Figure S4C.

Third, to uncover potential interaction interface(s) between Cirl isoforms and to control for unspecific hydrophobic interaction

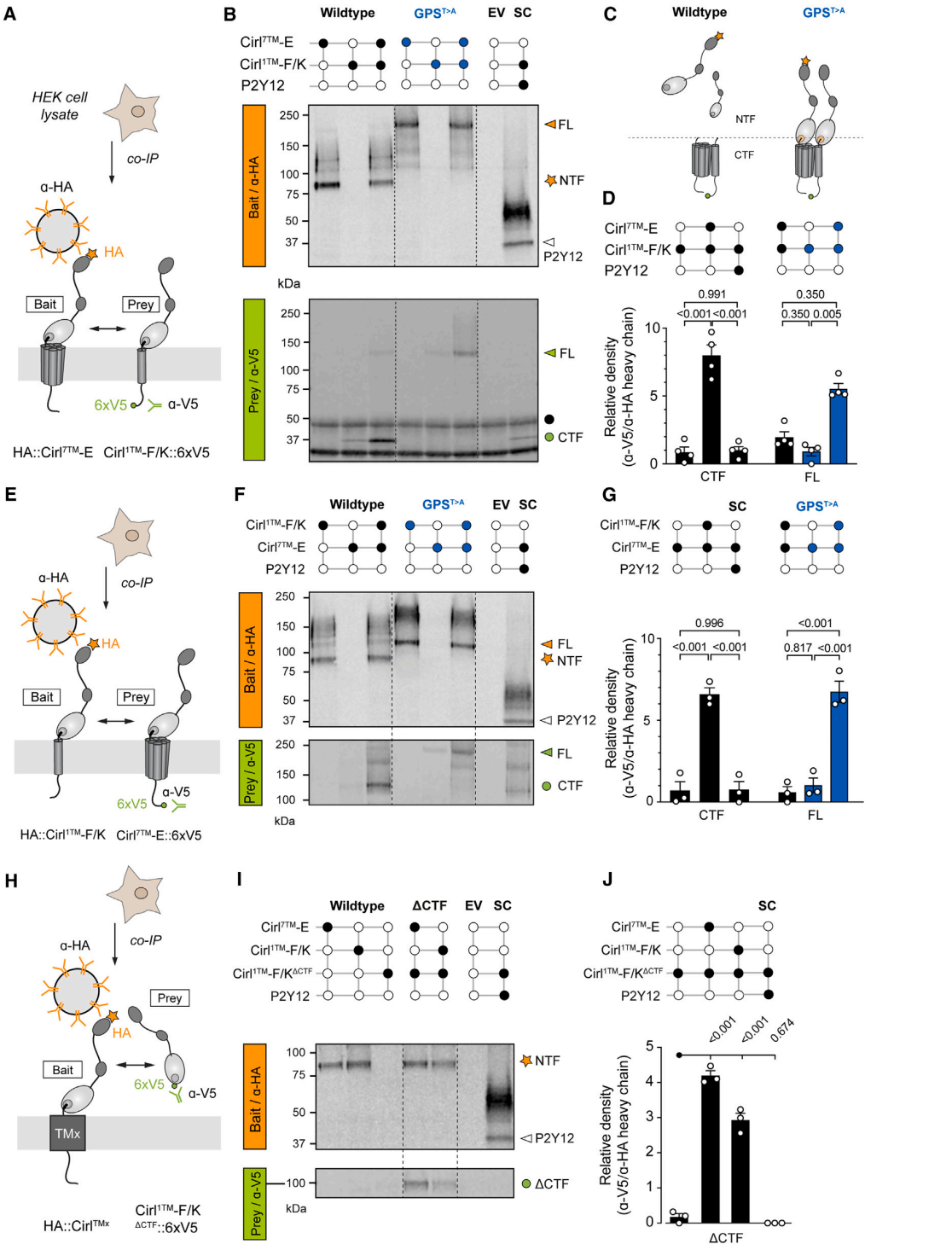

(legend on next page)

between the membrane-spanning α helices of Cirl^{7TM} and Cirl^{1TM}, we expressed a soluble NTF-only version of Cirl^{1TM}-F/K, lacking the CTF (Cirl^{1TM}-F/K$^{\Delta CTF}$::6xV5 (Figure 5H), as prey. Cirl^{1TM}-F/K$^{\Delta CTF}$ contains the same NTF layout as Cirl^{7TM}-E and Cirl^{1TM}-F/K (Figures S1A and S1B) and should, if precipitation occurs through the NTF, be able to co-immunoprecipitate with both isoforms. Indeed, Cirl^{1TM}-F/K$^{\Delta CTF}$::6xV5 (NTF, ~100 kDa) co-immunoprecipitated with either HA::Cirl^{7TM} or HA::Cirl^{1TM} but not with P2Y12 (Figures 5I and 5J). Quantification revealed a 24- or 17-fold increase in signal intensity of Cirl^{1TM}-F/K$^{\Delta CTF}$::6xV5 when co-expressed with HA::Cirl^{7TM} or HA::Cirl^{1TM}, respectively, as compared to its solitary expression (Figure 5J; Table S13). Hence, Cirl^{1TM}-F/K$^{\Delta CTF}$ suffices to bind Cirl^{7TM}-E (input samples in Figure S4D). In sum, these findings suggest the formation of heteromeric and potentially homomeric Cirl isoform complexes that occur independently of self-cleavage and that involve the NTF.

Cirl constitutes an ancient member of the aGPCR family.[10] Bioinformatics analyses predict the existence of 1TM transcripts derived from alternative splicing of evolutionarily younger aGPCR genes of mammalian genomes, including the Cirl homolog ADGRL1/LPHN1 (subfamily I), ADGRE5/CD97 (subfamily II), and ADGRG6/GPR126 (subfamily VIII).[17]

To get an idea whether isoform-specific complex assembly is conserved in mammalian aGPCRs and might occur for aGPCRs beyond subfamily I, we followed the bioinformatics[16,17] and cloned a tagged version of the predicted ADGRG6/GPR126^{1TM} protein from subfamily VIII (G6^{1TM}::6xV5) for coIP analyses with G6^{7TM} (HA::G6^{7TM}; Figure S6A). Both proteins were robustly expressed in HEK293T cells, and part of the ECR (ECR^{fragment}) of HA::G6^{7TM} and an FL G6^{1TM}::6xV5 protein were found in the input sample (Figure S6B). Intriguingly, FL and a fragment of the ICR (ICR^{fragment}) that corresponds to the CTF of G6^{1TM}::6xV5 co-immunoprecipitated with HA::G6^{7TM} bait when co-expressed, while no signal was detected when G6^{1TM}::6xV5 was expressed alone (Figures S6C and S6D; Table S14). When GAIN domain self-cleavage of HA::G6^{7TM} and G6^{1TM}::6xV5 was disabled, coIP still captured FL G6^{1TM}::6xV5 protein but, as expected, no ICR^{fragment} (Figures S6C and S6D; Table S14). Importantly, G6^{1TM}::6xV5 was not detected with P2Y12 as bait, confirming the specificity of the G6^{1TM}-G6^{7TM} interaction (Figure S6C and S6D; Table S14). These findings support the notion that complex assembly between isoforms may be a more general theme among aGPCRs.

Cirl-ECR and Cirl^{7TM} suffice to restore regular neuronal mechanosensitivity

Our coIP analyses suggest that the Cirl-NTF mediates, at least in part, the interaction between different Cirl isoforms (Figures 5I and 5J). Consequently, we asked whether the Cirl-NTF and Cirl^{7TM} constitute a functional unit required for neuronal mechanosensing precision. Therefore, we co-expressed Cirl^{7TM} together with Cirl-ECR (ECR includes the NTF) anchored within the plasma membrane through the TM of mouse CD8 (Cirl^{ECR}::mCD8^{TM}; Figure 6A) and recorded the mechanoresponse of lch5 neurons. Note that both Cirl^{ECR}::mCD8^{TM} and Cirl^{7TM} are expressed from the native *Cirl* promoter. Strikingly, the mechanosensitivity of sensory neurons in *Cirl^{ECR}::mCD8^{TM}/Cirl^{KO}* animals mirrored that in *Cirl^{KO}*, whereas *Cirl^{ECR}::mCD8^{TM}* in combination with *Cirl^{7TM}* rescued the mechanodiscrimination deficit (Figures 6B and 6C; Tables S20 and S21). Previously, we demonstrated that soluble NTF derived from a chimeric protein containing the Cirl-ECR and a juxta- and transmembrane segment of Notch suffices to bind the TLR-8/Tollo receptor in the larval central nervous system, a process pivotal for regulating neuroblast quantity.[11] Here, we show that the interplay between the Cirl-ECR and its conventional "sister" isoforms is essential for sensory precision of neurons in response to mechanical stimulation *in vivo*.

Figure 5. Cirl^{1TM}-NTF binds Cirl^{7TM}

(A) Schematic of coIP from heterologous HEK293T cells expressing Cirl^{7TM} as bait to capture Cirl^{1TM} prey (related to B–D).

(B) Immunoblot of coIP using wild-type or cleavage-deficient Cirl^{7TM} as bait (HA::Cirl^{7TM}-E and HA::Cirl^{7TM}-E$^{GPS/T>A}$). Presence and absence of proteins are indicated by filled and empty circles, respectively, above the blots. Immobilization and detection were done using anti-HA antibody. Cirl^{1TM}-F/K::6xV5 prey was detected using an anti-V5 antibody. FL HA::Cirl^{7TM}-E (~230 kDa): orange arrowhead. NTF of HA::Cirl^{7TM}-E (~90 kDa): orange star. FL Cirl^{1TM}-F/K::6xV5 (~130 kDa): green arrowhead. CTF of Cirl^{1TM}-F/K:6xV5 (~40 kDa): green circle. SC (specificity control): Cirl^{1TM}-F/K + P2Y12 (white arrowhead, ~40 kDa). A band of anti-HA antibody heavy chain (black circle) was used for normalization (D).

(C) Illustration of wild-type and cleavage-deficient Cirl isoforms detected in (B) and quantified in (D).

(D) Quantification of coIP signals as relative densities (STAR Methods) showed robust interaction between wild-type (black) and cleavage-deficient (blue) HA::Cirl^{7TM}-E and Cirl^{1TM}-F/K::6xV5 (N = 4). See also Tables S9 and S10.

(E) Schematic of coIP using an inverse strategy; i.e., with Cirl^{1TM} as bait to capture Cirl^{7TM} (related to F and G).

(F) Immunoblot of coIP using wild-type or cleavage-deficient Cirl^{1TM} as bait (HA::Cirl^{1TM}-F/K and HA::Cirl^{1TM}-F/K$^{GPS/T>A}$) and Cirl^{7TM}-E::6xV5 as prey. FL HA::Cirl^{1TM}-F/K (~110 kDa): orange arrowhead. NTF of HA::Cirl^{1TM}-F/K (~90 kDa): orange star. FL Cirl^{7TM}-E::6xV5 (~220 kDa): green arrowhead. CTF of Cirl^{7TM}-E::6xV5 (~130 kDa): green circle. SC: P2Y12 (white arrowhead, ~40 kDa) + Cirl^{7TM}-E.

(G) Quantification of coIP signals suggest interaction between wild-type (black) and cleavage-deficient (blue) HA::Cirl^{1TM}-F/K and Cirl^{7TM}-E::6xV5 (N = 3). Normalization of signal intensities as in (D). See also Tables S11 and S12.

(H) Schematic of coIP with membrane-anchored HA::Cirl^{TMx} (HA::Cirl^{1TM}-F/K or HA::Cirl^{7TM}-E) as bait to capture soluble Cirl-NTF::6xV5 (=ΔCTF).

(I) Immunoblot of coIP. Immobilization and detection of HA::Cirl^{TMx} (i.e., HA::Cirl^{1TM}-F/K or HA::Cirl^{7TM}-E) via anti-HA antibody (~90 kDa): orange star. Cirl^{1TM}-F/K$^{\Delta CTF}$::6xV5 was detected using anti-V5 antibody (~100 kDa): green circle. SC: P2Y12 (white arrowhead, ~40 kDa) + Cirl^{1TM}-F/K$^{\Delta CTF}$::6xV5.

(J) Quantification of coIP signals (I) suggest an NTF-dependent interaction between different isoforms (N = 3). Normalization of signal intensities as in (D). See also Table S13.

(B, F, and I) EV (empty vector): beads incubated with lysate from empty vector-transfected cells. Blots of input samples and tubulin (anti-Tubβ) as a loading control are shown in Figures S4B–S4D.

(D, G, and J) Data are displayed as mean ± SEM; p values are indicated.

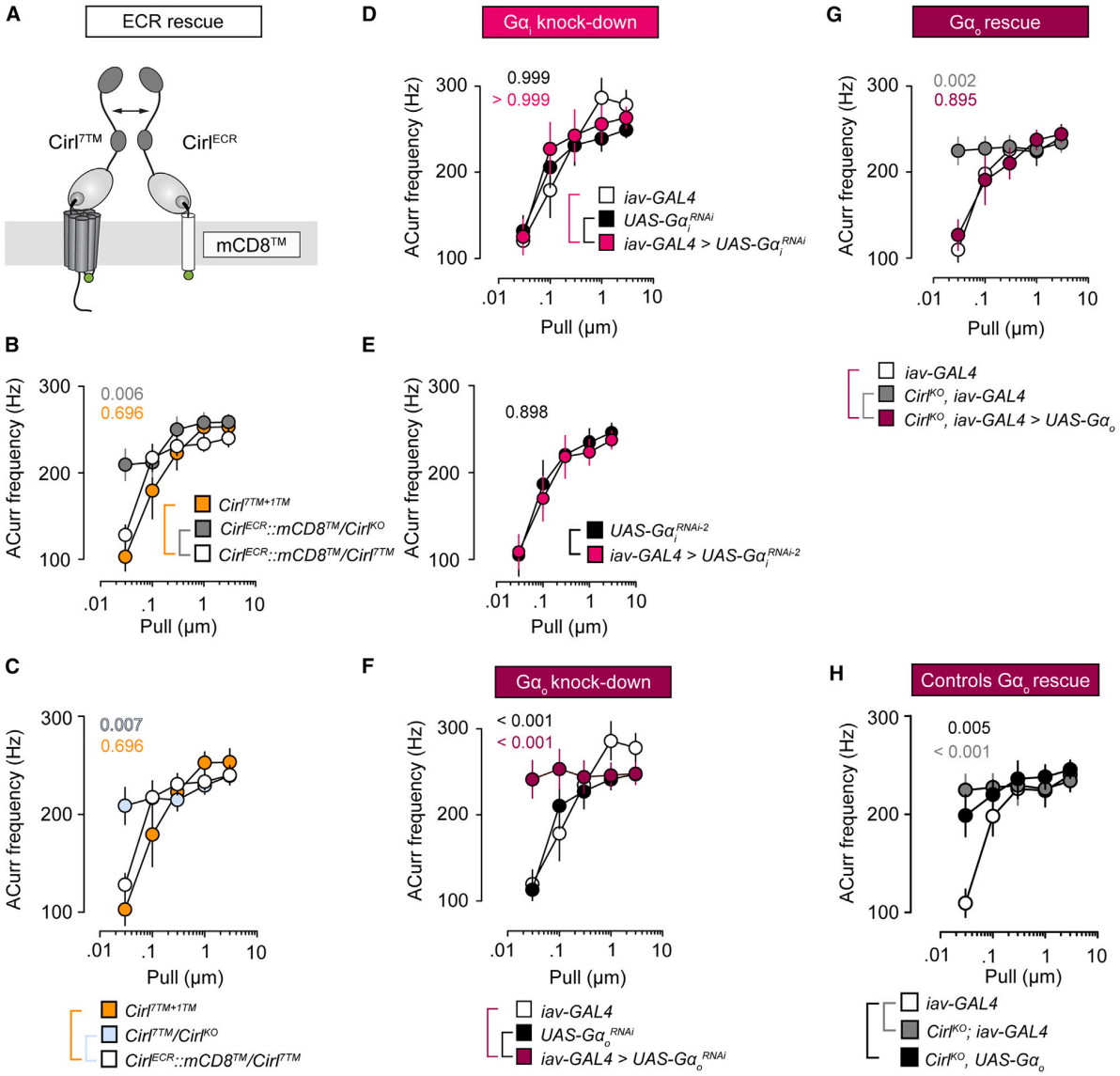

Figure 6. Cirl-ECR suffices to restore regular Ich5 mechanosensitivity through Cirl^{7TM}-Gα_o-dependent signaling

(A) Illustration of the ECR rescue experiment shown in (B) and (C). Cirl^{7TM} and Cirl^{ECR}::mCD8^{TM} contain a 2xV5 and 6xV5 tag (both shown in green), respectively.

(B–H) Quantification of ACurr frequencies from mechanically stimulated Ich5 neurons. Data are shown as mean ± SEM (each genotype $N = 10$). The p values derived from statistical comparison of ACurr frequencies at 30 nm pulls.

(B) Co-expression of Cirl^{7TM} and Cirl^{ECR}::mCD8^{TM} (including Cirl-NTF, white) restores Ich5 mechanosensitivity to wild-type levels. See also Tables S20 and S21.

(C) Cirl^{7TM} alone is not sufficient to rescue mechanosensitivity in *Cirl^{KO}* (blue) Ich5 neurons back to wild-type levels. See also Tables S20 and S21.

(D) Ich5 neuron-specific Gα_i knockdown leaves ACurr frequencies unaffected (pink). See also Tables S15 and S16.

(E) Gα_i knockdown with a second RNA$_i$ line leaves ACurr frequencies unaffected (pink). See also Table S17.

(F) Ich5 neuron-specific Gα_o knockdown (violet) increases in ACurr frequencies at 30 nm pulls, phenocopying the *Cirl^{KO}*. See also Tables S15 and S16.

(G) Ich5-specific overexpression of Gα_o (violet) rescues the elevated ACurr frequency of *Cirl^{KO}* back to control levels. See also Tables S18 and S19.

(H) *Cirl^{KO}* with one copy of *iav-GAL4* (gray) or *UAS-Gα_o* (black) does not restore ACurr frequencies. See also Tables S18 and S19.

Cirl modulates the sensitivity of mechanosensory neurons through Gα_o

Previous work has shown that Cirl affects Ich5 mechanosensing through cyclic AMP (cAMP)-dependent signaling.[25] Cirl^{1TM} proteins are ill-equipped to couple G proteins and are most likely unfit to act through inhibition of cAMP formation. To further substantiate that Cirl^{1TM} acts in conjunction with Cirl^{7TM}, we asked whether aberrant Ich5 mechanosensing in *Cirl^{7TM}* animals

(expressing Cirl^{7TM} but not Cirl^{1TM}; Figures 4D and 4G) is also related to elevated cAMP levels and can thus be reversed through pharmacological inhibition of adenylyl cyclases (ACs)[25] (Figure S5A). Application of the AC inhibitor SQ22536 (100 μM) rescued mechanically evoked ACurr frequencies in the absence of Cirl^{1TM} (*Cirl^{7TM}* animals) as well as in the absence of Cirl^{7TM} (*Cirl^{1TM}* animals) or both (*Cirl^{KO}* animals) (Figures S5B–S5D; Table S7). Importantly, mock incubation did not rescue ACurr frequencies (Figure S5E; Table S8). This dataset suggests that Cirl^{1TM} is involved in inhibiting cAMP production in mechanosensory neurons.

Previously, we have shown that overexpressed Cirl has the capacity to signal through Gα_i *in vitro.*[25] Gα_i protein is expressed in the developing lch5.[29] Hence, to test whether Gα_i signaling is relevant for mechanosensation *in vivo*, we knocked down *Gα_i* expression specifically in lch5 neurons using two different RNAi lines (*iav-GAL4 > UAS-Gα_i-RNAi-1* and *-2*). Surprisingly, we found no Gα_i-mediated effect on lch5 mechanoresponses (Figures 6D and 6E; Tables S15–S17).

Gα_o is known to play vital roles in different neuronal contexts.[30–34] When we measured the mechanoresponse of *Gα_o*-depleted lch5s (*iav-GAL4 > UAS-Gα_o-RNAi*), we found a phenocopy of *Cirl^{KO}* animals and isoform-specific *Cirl* mutants (Figure 6F; Tables S15 and S16). Consistent with this, lch5-specific neuronal overexpression of Gα_o in lch5 neurons of *Cirl^{KO}* animals (*Cirl^{KO}, iav-GAL4 > UAS-Gα_o*[33]) rescued the ACurr frequency phenotype (Figures 6G and 6H; Tables S18 and S19). These datasets show that Gα_o is a prerequisite of Cirl-dependent mechanosensing of lch5 neurons.

Together, our findings suggest a model where intron retention of the *Cirl* gene produces non-GPCR Cirl^{1TM} protein whose NTF can interact with Cirl^{7TM}-GPCR encoded in the same gene. This interaction appears to enable Gα_o-dependent signaling vital to tune the responsiveness of mechanosensory neurons.

DISCUSSION

While mechanosensing through ionotropic receptors is well recognized,[6] it is largely unknown how metabotropic receptors contribute to mechanosensitivity of neuronal tissues. Here, we show that *Cirl* uses intron retention as a physiological strategy to produce non-GPCR isoforms with a single TM and GPCR-like 7TM receptors from the same gene to enable tuning of neuronal mechanosensitivity.

Intron retention is a major alternative splicing mode[35] that is comparatively poorly understood[36] and is even often considered to be a consequence of erroneous splicing counteracted by nonsense-mediated mRNA decay.[37] Yet, intron retention has been reported to control developmentally regulated genes,[38] to curtail the abundance of protein-coding transcripts,[39] and as a mechanism to give rise to proteins with functions that appear to antagonize those of the original gene product.[40] Interestingly, intron retention of the GPCR gene encoding the glucose-dependent insulinotropic polypeptide receptor (GIPR), a class B GPCR, has been shown to produce mRNA in mouse islets that codes for GIPR-4TM isoforms. While the existence of such GIPR-4TM proteins has not been demonstrated *in vivo*, the authors show that heterologously overexpressed GIPR-4TM negatively affected surface trafficking of FL-GIPR in cell culture.[41] Collectively, these studies indicate the biological importance of intron retention. Here, we provide analyses of natively expressed mature transcripts with retained introns seen through to the functional level of the resulting protein isoforms in a living animal.

Homo- and heterodimerization of GPCRs is well established.[42–45] Previous investigations of conventional GPCRs in cell culture have also demonstrated the formation of complexes between truncated isoforms and their 7TM-GPCR counterparts.[46–53] These interactions have been found to exert positive[51–53] or negative effects on trafficking and/or signaling of the 7TM-GPCR *in vitro.*[41,46,47,49,50,54–59] Yet, native expression of truncated isoforms has been confirmed in only one of those studies.[51] The concept of dimerization is also known for aGPCRs[60–65]; however, so far, there has been no report on the formation of complexes among aGPCR isoforms, let alone a comprehensive analysis of their functional implications.

Here we studied the invertebrate ADGRL/*Cirl*, provide evidence of the expression of non-GPCR Cirl^{1TM} isoforms, and demonstrate the interaction of aGPCR isoforms. Our *in vivo* investigation of Cirl isoforms further showed that non-GPCR isoforms not only modulate 7TM-GPCR properties but are indispensable for 7TM-GPCR functionality and, thus, fundamental for shaping sensitivity to defined mechanical stimuli in individual neurons. Previous analysis of the aGPCR transcriptome hinted at the existence of non-GPCRs for vertebrate ADGRG6/GPR126. When we designed ADGRG6 isoforms based on this prediction and co-expressed it with GPCR-like ADGRG6 in HEK cells, we also found coIP. This finding supports the idea of isoform-specific complexation as a general phenomenon for aGPCR. At first glance, non-GPCR isoforms may be reminiscent of single-transmembrane GPCR-modulating proteins.[66] However, those are encoded in genes separate from those of the GPCRs they modulate.

GAIN domain-mediated self-cleavage of Cirl results in 7TM and 1TM isoforms, each consisting of non-covalently linked NTFs and CTFs. Remarkably, the mechanosensing capability of sensory neurons lacking Cirl was completely restored when the ECR of Cirl^{1TM} isoforms was co-expressed alongside the Cirl^{7TM} receptor *in vivo*. This suggests a mechanism where non-GPCR isoforms provide NTF; i.e., an interactor for metabotropic signaling through the GPCR-like 7TM isoforms. This is in line with prior work on homolog LAT-1 in *C. elegans* that showed stable ECR homodimer formation.[60] The sequences encoding the NTFs of different Cirl isoforms vary at the level of the RBL and GAIN domain. These variations may be a key determinant for intracellular trafficking and subcellular distribution of different isoforms and may underlie the combinatorial logic and specificity with which Cirl^{1TM}-deriving NTFs bind Cirl^{7TM} receptors.

Our previous findings established mechanical force as a trigger for the release of the Cirl-NTF and showed that glia-derived NTF controls the quantity of neuroblasts through Toll-like receptor 8/Tollo.[11,67] Hence, NTFs originating from non-GPCR-1TM sources (soluble or membrane attached) may be a physiological strategy that allows diverse complex compositions and signaling options when "paired" with aGPCR isoforms and other cell-surface molecules to convey signals within and across cells in a precise and selective fashion. This concept is

particularly intriguing in light of the extensive splice repertoire of aGPCR. Approximately 22% of mouse aGPCR genes yield transcripts that can potentially be translated into membrane-anchored NTFs and 56% into soluble NTFs.[17] In humans, even 45% of aGPCR genes have been reported to produce transcripts encoding membrane-anchored NTFs.[16]

The functional importance of non-GPCR proteins and other isoform types may also explain why previous rescue attempts of aGPCR knockout animal models with transgenes encoding only GPCR-like 7TM proteins were futile, whereas rescue strategies with genomic transgenes (which retain the ability to produce GPCR-like and non-GPCR isoforms) were successful.[10,68,69]

Our previous data suggested $G\alpha_i$ coupling of Cirl *in vitro*.[25] However, here we discovered a pathway dependent on $G\alpha_o$ to be pertinent for neuronal mechanosensing *in vivo*. Biased signaling, or functional selectivity, is a well-established concept for GPCRs,[70] and it is conceivable that Cirl can signal through $G\alpha_i$ in a different cellular context. Either way, the difference between *in vitro* and *in vivo* data highlights the importance of interpreting G protein signaling data with respect to expression conditions.

Finally, our results offer an explanation for the multifaceted splice repertoire of aGPCR genes: they might serve as a source of homophilic and potentially heterophilic interactors that enable metabotropic signaling via aGPCR proteins. These interactions may prove useful as means to interfere with aGPCR signaling and mechanosensitivity in the nervous system and other organs, offering promise for future development of pharmacological strategies.

Limitations of the study

Our study revealed the expression and *in vivo* function of unconventional 1TM-containing Cirl proteins. These proteins are co-expressed with conventional 7TM-containing ADGRL/Cirl isoforms. In the absence of either protein, regular neuronal mechanosensitivity is lost. This study provides evidence of the direct interaction between $Cirl^{1TM}$ and $Cirl^{7M}$ proteins; however, the stoichiometry of isoform complexes remains elusive. Future work is required to address these questions; e.g., using fluorescence resonance energy transfer (FRET) measurements *in vivo* in relevant tissues. Moreover, in this study, we discriminate between two isoform types ($Cirl^{1TM}$ vs. $Cirl^{7TM}$), but not between individual isoforms within these groups, as their sequences are very similar, escaping available genetic and immunohistochemical detection strategies. Non-GPCR/1TM transcripts have been predicted for several aGPCRs, including ADGRG6/GPR126. Similar to Cirl, we show interaction between 1TM and 7TM versions of ADGRG6 when overexpressed in cell culture. However, endogenous expression of $ADGRG6^{1TM}$ protein remains to be demonstrated, and further experiments are needed to determine whether the expression of non-GPCR proteins is truly a common physiological strategy among aGPCRs.

RESOURCE AVAILABILITY

Lead contact

Requests for further information, resources, and reagents should be directed to and will be fulfilled by the lead contact, Nicole Scholz (scholzlab@gmail.com).

Materials availability

Plasmids and fly strains generated in this study are available upon request.

Data and code availability

- All data are available from the lead contact upon request.
- This paper does not report original code.
- Any additional information required to reanalyze the data reported in this work paper is available from the lead contact upon request.

ACKNOWLEDGMENTS

We thank Maria Oppmann, Uta Strobel, Lena Abicht, Andrea Böhme, and Paula Beckmann for technical assistance; Vladimir Katanaev for materials; and Bertram Gerber, Robert Serfling, and Diana Le Duc for discussions. This work was supported by grants from the Deutsche Forschungsgemeinschaft (DFG) to N.S. and T.L. through FOR2149, Project P01 (project 265903901), CRC 1423 project B06 (project 421152132), T.L. through FOR2149, and Project P03 (project 265996823), T.S. CRC 1423 project C04 (project 421152132). M.B.K. was partially funded through the Else Kröner-Fresenius-Stiftung (2020_EKEA.42 to Diana Le Duc) and N.S. and D.L. through Junior research grants from the Medical Faculty, Leipzig University. Stocks obtained from the Bloomington Drosophila Stock Center (NIH P40OD018537) and Vienna Drosophila Resource Center (VDRC) were used in this study. Due to affiliation with Leipzig University, the open access publication costs were covered under the agreement between the DEAL consortium and Elsevier.

AUTHOR CONTRIBUTIONS

N.S. and D.L. conceived and supervised the study; prepared the figures, and wrote the manuscript with consent from all co-authors. Conceptualization, N.S., D.L., and T.L.; methodology, N.S., D.L., M.T., M.S., M.B., M.B.K., J.I., T.L., J.L., M.S.G., and J.A.; validation, N.S., D.L., M.B., M.B.K., A.B., and A.-K.D.; formal analysis, N.S., D.L., M.T., M.S., M.B., A.B., M.B.K., J.I., A.-K.D., T.L., and M.S.G.; investigation, N.S., D.L., T.S., V.L., M.B., A.B., M.B.K., E.K., J.I., D.C.N.H., A.K.D., T.L., J.L., M.S.G., and J.A.; writing – original draft, N.S. and D.L.; writing – review & editing, N.S., D.L., T.L., T.S., A.B., M.B.K., A.K.D., and J.L.; visualization, N.S., D.L., and A.B.; supervision N.S. and D.L.; project administration, N.S. and T.L.; funding acquisition, N.S., D.L., T.L., and T.S.

DECLARATION OF INTERESTS

The authors declare no competing interests.

DECLARATION OF GENERATIVE AI AND AI-ASSISTED TECHNOLOGIES IN THE WRITING PROCESS

During the preparation of this manuscript, the authors used ChatGTP v.3.5 (free online version) to improve language and readability. After using this tool, the authors reviewed and edited the content as needed and take full responsibility for the content of the publication.

STAR★METHODS

Detailed methods are provided in the online version of this paper and include the following:

- KEY RESOURCES TABLE
- EXPERIMENTAL MODEL AND STUDY PARTICIPANT DETAILS
  - *Drosophila* stock and culture
- METHOD DETAILS
  - Molecular cloning
  - PhiC31-mediated integration of transgenes
  - RT-PCR
  - RNA-sequencing analyses
  - Cell culture
  - Immunofluorescence and imaging

SUPPLEMENTAL INFORMATION

Supplemental information can be found online at https://doi.org/10.1016/j.celrep.2024.115078.

Received: January 31, 2024
Revised: November 13, 2024
Accepted: November 26, 2024

REFERENCES

1. Yang, D., Zhou, Q., Labroska, V., Qin, S., Darbalaei, S., Wu, Y., Yuliantie, E., Xie, L., Tao, H., Cheng, J., et al. (2021). G protein-coupled receptors: structure- and function-based drug discovery. Signal Transduct. Target. Ther. *6*, 7. https://doi.org/10.1038/s41392-020-00435-w.
2. Hamann, J., Aust, G., Araç, D., Engel, F.B., Formstone, C., Fredriksson, R., Hall, R.A., Harty, B.L., Kirchhoff, C., Knapp, B., et al. (2015). International Union of Basic and Clinical Pharmacology. XCIV. Adhesion G protein-coupled receptors. Pharmacol. Rev. *67*, 338–367. https://doi.org/10.1124/pr.114.009647.
3. Petersen, S.C., Luo, R., Liebscher, I., Giera, S., Jeong, S.-J., Mogha, A., Ghidinelli, M., Feltri, M.L., Schöneberg, T., Piao, X., and Monk, K.R. (2015). The Adhesion GPCR GPR126 Has Distinct, Domain-Dependent Functions in Schwann Cell Development Mediated by Interaction with Laminin-211. Neuron *85*, 755–769. https://doi.org/10.1016/j.neuron.2014.12.057.
4. White, J.P., Wrann, C.D., Rao, R.R., Nair, S.K., Jedrychowski, M.P., You, J.S., Martínez-Redondo, V., Gygi, S.P., Ruas, J.L., Hornberger, T.A., et al. (2014). G protein-coupled receptor 56 regulates mechanical overload-induced muscle hypertrophy. Proc. Natl. Acad. Sci. USA *111*, 15756–15761. https://doi.org/10.1073/pnas.1417898111.
5. Boyden, S.E., Desai, A., Cruse, G., Young, M.L., Bolan, H.C., Scott, L.M., Eisch, A.R., Long, R.D., Lee, C.-C.R., Satorius, C.L., et al. (2016). Vibratory Urticaria Associated with a Missense Variant in ADGRE2. N. Engl. J. Med. *374*, 656–663. https://doi.org/10.1056/nejmoa1500611.
6. Scholz, N., Monk, K.R., Kittel, R.J., and Langenhan, T. (2016). Adhesion GPCRs as a Putative Class of Metabotropic Mechanosensors. Handb. Exp. Pharmacol. *234*, 221–247. https://doi.org/10.1007/978-3-319-41523-9_10.
7. Wilde, C., Fischer, L., Lede, V., Kirchberger, J., Rothemund, S., Schöneberg, T., and Liebscher, I. (2016). The constitutive activity of the adhesion GPCR GPR114/ADGRG5 is mediated by its tethered agonist. FASEB J *30*, 666–673. https://doi.org/10.1096/fj.15-276220.
8. Liu, D., Duan, L., Rodda, L.B., Lu, E., Xu, Y., An, J., Qiu, L., Liu, F., Looney, M.R., Yang, Z., et al. (2022). CD97 promotes spleen dendritic cell homeostasis through the mechanosensing of red blood cells. Science *375*, eabi5965. https://doi.org/10.1126/science.abi5965.
9. Lin, H.-H., Ng, K.-F., Chen, T.-C., and Tseng, W.-Y. (2022). Ligands and Beyond: Mechanosensitive Adhesion GPCRs. Pharmaceuticals *15*, 219. https://doi.org/10.3390/ph15020219.
10. Scholz, N., Gehring, J., Guan, C., Ljaschenko, D., Fischer, R., Lakshmanan, V., Kittel, R.J., and Langenhan, T. (2015). The Adhesion GPCR Latrophilin/CIRL Shapes Mechanosensation. Cell Rep. *11*, 866–874. https://doi.org/10.1016/j.celrep.2015.04.008.
11. Scholz, N., Dahse, A.-K., Kemkemer, M., Bormann, A., Auger, G.M., Vieira Contreras, F., Ernst, L.F., Staake, H., Körner, M.B., Buhlan, M., et al. (2023). Molecular sensing of mechano- and ligand-dependent adhesion GPCR dissociation. Nature *615*, 945–953. https://doi.org/10.1038/s41586-023-05802-5.
12. Liebscher, I., Cevheroğlu, O., Hsiao, C.-C., Maia, A.F., Schihada, H., Scholz, N., Soave, M., Spiess, K., Trajković, K., Kosloff, M., et al. (2022). A guide to adhesion GPCR research. FEBS J. *289*, 7610–7630. https://doi.org/10.1111/febs.16258.
13. Koser, D.E., Thompson, A.J., Foster, S.K., Dwivedy, A., Pillai, E.K., Sheridan, G.K., Svoboda, H., Viana, M., Costa, L.d.F., Guck, J., et al. (2016). Mechanosensing is critical for axon growth in the developing brain. Nat. Neurosci. *19*, 1592–1598. https://doi.org/10.1038/nn.4394.
14. Tyler, W.J. (2012). The mechanobiology of brain function. Nat. Rev. Neurosci. *13*, 867–878. https://doi.org/10.1038/nrn3383.
15. Chighizola, M., Dini, T., Lenardi, C., Milani, P., Podestà, A., and Schulte, C. (2019). Mechanotransduction in neuronal cell development and functioning. Biophys. Rev. *11*, 701–720. https://doi.org/10.1007/s12551-019-00587-2.
16. Kuhn, C.K., Stenzel, U., Berndt, S., Liebscher, I., Schöneberg, T., and Horn, S. (2024). The repertoire and structure of adhesion GPCR transcript variants assembled from publicly available deep-sequenced human samples. Nucleic Acids Res. *52*, 3823–3836. https://doi.org/10.1093/nar/gkae145.
17. Knierim, A.B., Röthe, J., Çakir, M.V., Lede, V., Wilde, C., Liebscher, I., Thor, D., and Schöneberg, T. (2019). Genetic basis of functional variability in adhesion G protein-coupled receptors. Sci. Rep. *9*, 11036. https://doi.org/10.1038/s41598-019-46265-x.
18. Araç, D., Boucard, A.A., Bolliger, M.F., Nguyen, J., Soltis, S.M., Südhof, T.C., and Brunger, A.T. (2012). A novel evolutionarily conserved domain of cell-adhesion GPCRs mediates autoproteolysis. EMBO J. *31*, 1364–1378. https://doi.org/10.1038/emboj.2012.26.
19. Wang, Y., Cao, Y., Hays, C.L., Laboute, T., Ray, T.A., Guerrero-Given, D., Ahuja, A.S., Patil, D., Rivero, O., Kamasawa, N., et al. (2021). Adhesion GPCR Latrophilin 3 regulates synaptic function of cone photoreceptors in a trans-synaptic manner. Proc National Acad Sci *118*, e2106694118. https://doi.org/10.1073/pnas.2106694118.
20. Wang, S., DeLeon, C., Sun, W., Quake, S.R., Roth, B.L., and Südhof, T.C. (2024). Alternative splicing of latrophilin-3 controls synapse formation. Nature *626*, 128–135. https://doi.org/10.1038/s41586-023-06913-9.
21. Li, T., Luo, R., Schmidt, R., D'Alessandro, N., Kishore, P., Zhu, B., Yu, D., and Piao, X. (2023). GPR56 S4 variant is required for microglia-mediated synaptic pruning. Glia *71*, 560–570. https://doi.org/10.1002/glia.24293.
22. Monteuuis, G., Wong, J.J.L., Bailey, C.G., Schmitz, U., and Rasko, J.E.J. (2019). The changing paradigm of intron retention: regulation, ramifications and recipes. Nucleic Acids Res. *47*, 11497–11513. https://doi.org/10.1093/nar/gkz1068.
23. Graveley, B.R., Brooks, A.N., Carlson, J.W., Duff, M.O., Landolin, J.M., Yang, L., Artieri, C.G., van Baren, M.J., Boley, N., Booth, B.W., et al. (2011). The developmental transcriptome of Drosophila melanogaster. Nature *471*, 473–479. https://doi.org/10.1038/nature09715.
24. Lavalou, J., Mao, Q., Harmansa, S., Kerridge, S., Lellouch, A.C., Philippe, J.-M., Audebert, S., Camoin, L., and Lecuit, T. (2021). Formation of polarized contractile interfaces by self-organized Toll-8/Cirl GPCR asymmetry. Dev. Cell *56*, 1574–1588.e7. https://doi.org/10.1016/j.devcel.2021.03.030.
25. Scholz, N., Guan, C., Nieberler, M., Grotemeyer, A., Maiellaro, I., Gao, S., Beck, S., Pawlak, M., Sauer, M., Asan, E., et al. (2017). Mechano-dependent signaling by Latrophilin/CIRL quenches cAMP in proprioceptive neurons. Elife *6*, e28360. https://doi.org/10.7554/elife.28360.
26. Nieberler, M., Kittel, R.J., Petrenko, A.G., Lin, H.-H., and Langenhan, T. (2016). Control of Adhesion GPCR Function Through Proteolytic Processing. In Adhesion G Protein-coupled Receptors: Molecular, Physiological

and Pharmacological Principles in Health and Disease, *Volume 234*, T. Langenhan and T. Schöneberg, eds. (Springer), pp. 83–109. https://doi.org/10.1007/978-3-319-41523-9_5.

27. Caldwell, J.C., Miller, M.M., Wing, S., Soll, D.R., and Eberl, D.F. (2003). Dynamic analysis of larval locomotion in Drosophila chordotonal organ mutants. Proc. Natl. Acad. Sci. USA *100*, 16053–16058. https://doi.org/10.1073/pnas.2535546100.
28. Dana, H., Sun, Y., Mohar, B., Hulse, B.K., Kerlin, A.M., Hasseman, J.P., Tsegaye, G., Tsang, A., Wong, A., Patel, R., et al. (2019). High-performance calcium sensors for imaging activity in neuronal populations and microcompartments. Nat Meth *16*, 649–657. https://doi.org/10.1038/s41592-019-0435-6.
29. Wolfgang, W.J., Quan, F., Thambi, N., and Forte, M. (1991). Restricted spatial and temporal expression of G-protein alpha subunits during Drosophila embryogenesis. Development *113*, 527–538.
30. Wolfgang, W.J., Quan, F., Goldsmith, P., Unson, C., Spiegel, A., and Forte, M. (1990). Immunolocalization of G protein alpha-subunits in the Drosophila CNS. J. Neurosci. *10*, 1014–1024. https://doi.org/10.1523/jneurosci.10-03-01014.1990.
31. Sternweis, P.C., and Robishaw, J.D. (1984). Isolation of two proteins with high affinity for guanine nucleotides from membranes of bovine brain. J. Biol. Chem. *259*, 13806–13813.
32. Strittmatter, S.M., Fishman, M.C., and Zhu, X.P. (1994). Activated mutants of the alpha subunit of G(o) promote an increased number of neurites per cell. J. Neurosci. *14*, 2327–2338. https://doi.org/10.1523/jneurosci.14-04-02327.1994.
33. Solis, G.P., Bilousov, O., Koval, A., Lüchtenborg, A.-M., Lin, C., and Katanaev, V.L. (2017). Golgi-Resident Gαo Promotes Protrusive Membrane Dynamics. Cell *170*, 939–955.e24. https://doi.org/10.1016/j.cell.2017.07.015.
34. Muntean, B.S., Masuho, I., Dao, M., Sutton, L.P., Zucca, S., Iwamoto, H., Patil, D.N., Wang, D., Birnbaumer, L., Blakely, R.D., et al. (2021). Gαo is a major determinant of cAMP signaling in the pathophysiology of movement disorders. Cell Rep. *34*, 108718. https://doi.org/10.1016/j.celrep.2021.108718.
35. Wang, E.T., Sandberg, R., Luo, S., Khrebtukova, I., Zhang, L., Mayr, C., Kingsmore, S.F., Schroth, G.P., and Burge, C.B. (2008). Alternative isoform regulation in human tissue transcriptomes. Nature *456*, 470–476. https://doi.org/10.1038/nature07509.
36. Braunschweig, U., Barbosa-Morais, N.L., Pan, Q., Nachman, E.N., Alipanahi, B., Gonatopoulos-Pournatzis, T., Frey, B., Irimia, M., and Blencowe, B.J. (2014). Widespread intron retention in mammals functionally tunes transcriptomes. Genome Res. *24*, 1774–1786. https://doi.org/10.1101/gr.177790.114.
37. Wong, J.J.-L., Ritchie, W., Ebner, O.A., Selbach, M., Wong, J.W.H., Huang, Y., Gao, D., Pinello, N., Gonzalez, M., Baidya, K., et al. (2013). Orchestrated intron retention regulates normal granulocyte differentiation. Cell *154*, 583–595. https://doi.org/10.1016/j.cell.2013.06.052.
38. Yap, K., Lim, Z.Q., Khandelia, P., Friedman, B., and Makeyev, E.V. (2012). Coordinated regulation of neuronal mRNA steady-state levels through developmentally controlled intron retention. Genes Dev. *26*, 1209–1223. https://doi.org/10.1101/gad.188037.112.
39. Gill, J., Park, Y., McGinnis, J.P., Perez-Sanchez, C., Blanchette, M., and Si, K. (2017). Regulated Intron Removal Integrates Motivational State and Experience. Cell *169*, 836–848.e15. https://doi.org/10.1016/j.cell.2017.05.006.
40. Gontijo, A.M., Miguela, V., Whiting, M.F., Woodruff, R.C., and Dominguez, M. (2011). Intron retention in the Drosophila melanogaster Rieske Iron Sulphur Protein gene generated a new protein. Nat. Commun. *2*, 323. https://doi.org/10.1038/ncomms1328.
41. Harada, N., Yamada, Y., Tsukiyama, K., Yamada, C., Nakamura, Y., Mukai, E., Hamasaki, A., Liu, X., Toyoda, K., Seino, Y., and Inagaki, N. (2008). A novel GIP receptor splice variant influences GIP sensitivity of pancreatic β-cells in obese mice. Am. J. Physiol. Endocrinol. Metab. *294*, E61–E68. https://doi.org/10.1152/ajpendo.00358.2007.
42. Lohse, M.J. (2010). Dimerization in GPCR mobility and signaling. Curr. Opin. Pharmacol. *10*, 53–58. https://doi.org/10.1016/j.coph.2009.10.007.
43. Limbird, L.E., Meyts, P.D., and Lefkowitz, R.J. (1975). Beta-adrenergic receptors: evidence for negative cooperativity. Biochem. Biophys. Res. Commun. *64*, 1160–1168. https://doi.org/10.1016/0006-291x(75)90815-3.
44. Faron-Górecka, A., Szlachta, M., Kolasa, M., Solich, J., Górecki, A., Kusmider, M., Zurawek, D., and Dziedzicka-Wasylewska, M. (2019). Understanding GPCR dimerization. In G Protein-Coupled Receptors 2nd Edition Part B, 2nd ed. (Academic Press: Cambridge). https://doi.org/10.1016/bs.mcb.2018.08.005.
45. Pin, J.-P., Neubig, R., Bouvier, M., Devi, L., Filizola, M., Javitch, J.A., Lohse, M.J., Milligan, G., Palczewski, K., Parmentier, M., and Spedding, M. (2007). International Union of Basic and Clinical Pharmacology. LXVII. Recommendations for the recognition and nomenclature of G protein-coupled receptor heteromultimers. Pharmacol. Rev. *59*, 5–13. https://doi.org/10.1124/pr.59.1.5.
46. Schwarz, D.A., Barry, G., Eliasof, S.D., Petroski, R.E., Conlon, P.J., and Maki, R.A. (2000). Characterization of γ-Aminobutyric Acid Receptor GABAB(1e), a GABAB(1) Splice Variant Encoding a Truncated Receptor. J. Biol. Chem. *275*, 32174–32181. https://doi.org/10.1074/jbc.m005333200.
47. Ding, W.-Q., Cheng, Z.-J., McElhiney, J., Kuntz, S.M., and Miller, L.J. (2002). Silencing of secretin receptor function by dimerization with a mis-spliced variant secretin receptor in ductal pancreatic adenocarcinoma. Cancer Res. *62*, 5223–5229.
48. Cheung, T.C., and Hearn, J.P. (2005). Dimerizations of the wallaby gonadotropin-releasing hormone receptor and its splice variants. Gen. Comp. Endocrinol. *144*, 280–288. https://doi.org/10.1016/j.ygcen.2005.06.008.
49. McElvaine, A.T., and Mayo, K.E. (2006). A Dominant-Negative Human Growth Hormone-Releasing Hormone (GHRH) Receptor Splice Variant Inhibits GHRH Binding. Endocrinology *147*, 1884–1894. https://doi.org/10.1210/en.2005-1488.
50. Córdoba-Chacón, J., Gahete, M.D., Durán-Prado, M., Luque, R.M., and Castaño, J.P. (2011). Truncated somatostatin receptors as new players in somatostatin–cortistatin pathophysiology. Ann. N. York Acad. Sci. *1220*, 6–15. https://doi.org/10.1111/j.1749-6632.2011.05985.x.
51. Bagher, A.M., Laprairie, R.B., Kelly, M.E.M., and Denovan-Wright, E.M. (2013). Co-expression of the human cannabinoid receptor coding region splice variants (hCB_4) affects the function of hCB_1 receptor complexes. Eur. J. Pharmacol. *721*, 341–354. https://doi.org/10.1016/j.ejphar.2013.09.002.
52. Wang, C., Pan, Y., Zhang, R., Bai, B., Chen, J., and Randeva, H.S. (2014). Heterodimerization of Mouse Orexin type 2 receptor variants and the effects on signal transduction. Biochim. Biophys. Acta *1843*, 652–663. https://doi.org/10.1016/j.bbamcr.2013.12.010.
53. Zhang, T., Xu, J., and Pan, Y.-X. (2020). A truncated six transmembrane splice variant MOR-1G enhances expression of the full-length seven transmembrane mu opioid receptor through heterodimerization. Mol. Pharmacol. *98*, 518–527. https://doi.org/10.1124/mol.120.119453.
54. Grosse, R., Schöneberg, T., Schultz, G., and Gudermann, T. (1997). Inhibition of gonadotropin-releasing hormone receptor signaling by expression of a splice variant of the human receptor. Mol. Endocrinol. *11*, 1305–1318. https://doi.org/10.1210/mend.11.9.9966.
55. Oda, Y., Tu, C.-L., Pillai, S., and Bikle, D.D. (1998). The Calcium Sensing Receptor and Its Alternatively Spliced Form in Keratinocyte Differentiation. J. Biol. Chem. *273*, 23344–23352. https://doi.org/10.1074/jbc.273.36.23344.
56. Cogé, F., Guenin, S.P., Renouard-Try, A., Rique, H., Ouvry, C., Fabry, N., Beauverger, P., Nicolas, J.P., Galizzi, J.P., Boutin, J.A., et al. (1999).

Truncated isoforms inhibit [3H]prazosin binding and cellular trafficking of native human alpha1A-adrenoceptors. Biochem. J. 343 Pt *1*, 231–239.

57. Dickinson, R.E., Stewart, A.J., Myers, M., Millar, R.P., and Duncan, W.C. (2009). Differential Expression and Functional Characterization of Luteinizing Hormone Receptor Splice Variants in Human Luteal Cells: Implications for Luteolysis. Endocrinology *150*, 2873–2881. https://doi.org/10.1210/en.2008-1382.
58. Sanchez, C., Escrieut, C., Clerc, P., Gigoux, V., Waser, B., Reubi, J.C., and Fourmy, D. (2012). Characterization of a novel five-transmembrane domain cholecystokinin-2 receptor splice variant identified in human tumors. Mol. Cell. Endocrinol. *349*, 170–179. https://doi.org/10.1016/j.mce.2011.10.010.
59. Nakamura, K., Yamashita, S., Omori, Y., and Minegishi, T. (2004). A Splice Variant of the Human Luteinizing Hormone (LH) Receptor Modulates the Expression of Wild-Type Human LH Receptor. Mol. Endocrinol. *18*, 1461–1470. https://doi.org/10.1210/me.2003-0489.
60. Prömel, S., Frickenhaus, M., Hughes, S., Mestek, L., Staunton, D., Woollard, A., Vakonakis, I., Schöneberg, T., Schnabel, R., Russ, A.P., and Langenhan, T. (2012). The GPS motif is a molecular switch for bimodal activities of adhesion class G protein-coupled receptors. Cell Rep. *2*, 321–331. https://doi.org/10.1016/j.celrep.2012.06.015.
61. Volynski, K.E., Silva, J.P., Lelianova, V.G., Atiqur Rahman, M., Hopkins, C., and Ushkaryov, Y.A. (2004). Latrophilin fragments behave as independent proteins that associate and signal on binding of LTXN4C. Embo J *23*, 4423–4433. https://doi.org/10.1038/sj.emboj.7600443.
62. Nishiguchi, S., Kasai, R.S., and Uchihashi, T. (2023). Antiparallel dimer structure of CELSR cadherin in solution revealed by high-speed-atomic force microscopy. Proc. Natl. Acad. Sci. USA *120*, e2302047120. https://doi.org/10.1073/pnas.2302047120.
63. Nishimura, T., Honda, H., and Takeichi, M. (2012). Planar cell polarity links axes of spatial dynamics in neural-tube closure. Cell *149*, 1084–1097. https://doi.org/10.1016/j.cell.2012.04.021.
64. Abe, J., Suzuki, H., Notoya, M., Yamamoto, T., and Hirose, S. (1999). Ig-hepta, a novel member of the G protein-coupled hepta-helical receptor (GPCR) family that has immunoglobulin-like repeats in a long N-terminal extracellular domain and defines a new subfamily of GPCRs. J. Biol. Chem. *274*, 19957–19964.
65. Shima, Y., Kawaguchi, S.y., Kosaka, K., Nakayama, M., Hoshino, M., Nabeshima, Y., Hirano, T., and Uemura, T. (2007). Opposing roles in neurite growth control by two seven-pass transmembrane cadherins. Nat. Neurosci. *10*, 963–969. https://doi.org/10.1038/nn1933.
66. Wang, M., Lyu, J., and Zhang, C. (2024). Single transmembrane GPCR modulating proteins: neither single nor simple. Protein Cell *15*, 395–402. https://doi.org/10.1093/procel/pwad035.
67. Buhlan, M., Ljaschenko, D., Scholz, N., and Langenhan, T. (2024). Experimental modulation of physiological force application on leg joint neurons in intact Drosophila melanogaster. Nat. Protoc. *19*, 113–126. https://doi.org/10.1038/s41596-023-00907-7.
68. Langenhan, T., Prömel, S., Mestek, L., Esmaeili, B., Waller-Evans, H., Hennig, C., Kohara, Y., Avery, L., Vakonakis, I., Schnabel, R., and Russ, A.P. (2009). Latrophilin signaling links anterior-posterior tissue polarity and oriented cell divisions in the C. elegans embryo. Dev. Cell *17*, 494–504. https://doi.org/10.1016/j.devcel.2009.08.008.
69. Patra, C., van Amerongen, M.J., Ghosh, S., Ricciardi, F., Sajjad, A., Novoyatleva, T., Mogha, A., Monk, K.R., Mühlfeld, C., and Engel, F.B. (2013). Organ-specific function of adhesion G protein-coupled receptor GPR126 is domain-dependent. Proc. Natl. Acad. Sci. USA *110*, 16898–16903. https://doi.org/10.1073/pnas.1304837110.
70. Wisler, J.W., Rockman, H.A., and Lefkowitz, R.J. (2018). Biased G Protein-Coupled Receptor Signaling: Changing the Paradigm of Drug Discovery. Circulation *137*, 2315–2317. https://doi.org/10.1161/circulationaha.117.028194.
71. Kodama, Y., Shumway, M., and Leinonen, R.; International Nucleotide Sequence Database Collaboration (2012). The Sequence Read Archive: explosive growth of sequencing data. Nucleic Acids Res. *40*, D54–D56. https://doi.org/10.1093/nar/gkr854.
72. Langmead, B., Trapnell, C., Pop, M., and Salzberg, S.L. (2009). Ultrafast and memory-efficient alignment of short DNA sequences to the human genome. Genome Biol. *10*, R25. https://doi.org/10.1186/gb-2009-10-3-r25.
73. Li, H., Handsaker, B., Wysoker, A., Fennell, T., Ruan, J., Homer, N., Marth, G., Abecasis, G., and Durbin, R.; 1000 Genome Project Data Processing Subgroup (2009). The Sequence Alignment/Map format and SAMtools. Bioinformatics *25*, 2078–2079. https://doi.org/10.1093/bioinformatics/btp352.
74. Pertea, M., Pertea, G.M., Antonescu, C.M., Chang, T.-C., Mendell, J.T., and Salzberg, S.L. (2015). StringTie enables improved reconstruction of a transcriptome from RNA-seq reads. Nat. Biotechnol. *33*, 290–295. https://doi.org/10.1038/nbt.3122.
75. Pertea, M., Kim, D., Pertea, G.M., Leek, J.T., and Salzberg, S.L. (2016). Transcript-level expression analysis of RNA-seq experiments with HISAT, StringTie and Ballgown. Nat. Protoc. *11*, 1650–1667. https://doi.org/10.1038/nprot.2016.095.
76. Robinson, J.T., Thorvaldsdóttir, H., Winckler, W., Guttman, M., Lander, E.S., Getz, G., and Mesirov, J.P. (2011). Integrative genomics viewer. Nat. Biotechnol. *29*, 24–26. https://doi.org/10.1038/nbt.1754.
77. Thorvaldsdóttir, H., Robinson, J.T., and Mesirov, J.P. (2013). Integrative Genomics Viewer (IGV): high-performance genomics data visualization and exploration. Brief. Bioinform. *14*, 178–192. https://doi.org/10.1093/bib/bbs017.
78. Stewart, B.A., Atwood, H.L., Renger, J.J., Wang, J., and Wu, C.-F. (1994). Improved stability of Drosophila larval neuromuscular preparations in haemolymph-like physiological solutions. J. Comp. Physiol. *175*, 179–191. https://doi.org/10.1007/bf00215114.
79. Stael, S., Miller, L.P., Fernández-Fernández, Á.D., and Breusegem, F.V. (2022). Plant Proteases and Plant Cell Death, Methods and Protocols. Methods Mol. Biol. *2447*, 127–137. https://doi.org/10.1007/978-1-0716-2079-3_11.
80. Scholz, N., Ehmann, N., Sachidanandan, D., Imig, C., Cooper, B.H., Jahn, O., Reim, K., Brose, N., Meyer, J., Lamberty, M., et al. (2019). Complexin cooperates with Bruchpilot to tether synaptic vesicles to the active zone cytomatrix. J. Cell Biol. *218*, 1011–1026. https://doi.org/10.1083/jcb.201806155.
81. Wilson, R.I., Turner, G.C., and Laurent, G. (2004). Transformation of Olfactory Representations in the Drosophila Antennal Lobe. Science *303*, 366–370. https://doi.org/10.1126/science.1090782.

STAR★METHODS

KEY RESOURCES TABLE

REAGENT or RESOURCE	SOURCE	IDENTIFIER
Antibodies		
rabbit-anti-dsRed	Takara	RRID:AB_10013483
anti-HRP conjugated with Alexa Fluor 488	Jackson ImmunoResearch	RRID:AB_2338965
goat-anti-rabbit conjugated with Cy5	Jackson ImmunoResearch	RRID: AB_2338013
rabbit-anti-RFP	Antibodies-Online	RRID:AB_10781500
mouse-anti-V5	Invitrogen	RRID:AB_2556564
rabbit-anti-HA, C29F4	Cell Signaling Technology	RRID:AB_1549585
rabbit-anti-tubulinα	Santa Cruz Antibodies	#12462-R; RRID:AB_2241125
mouse-anti-tubulinβ, e7	Developmental Studies Hybridoma Bank	RRID: AB_528499
IRDye® 680RD Goat anti-Mouse IgG Secondary Antibody	LI-COR Biosciences	RRID: AB_10956588
IRDye® 680RD Goat anti-Rabbit IgG Secondary Antibody	LI-COR Biosciences	RRID: AB_10956166
IRDye® 800CW Goat anti-Mouse IgG Secondary Antibody	LI-COR Biosciences	RRID: AB_621842
IRDye® 800CW Goat anti-Rabbit IgG Secondary Antibody	LI-COR Biosciences	RRID: AB_621843
Bacterial and virus strains		
E. coli XL1-Blue Competent Cells	Agilent	#200236
NEB® 5-alpha Competent *E. coli* (High Efficiency)	NEB	#C2987I
CopyCutter™EPI400™ Chemically Competent *E. coli*	Lucigen	#C400CH10
Chemicals, peptides, and recombinant proteins		
Ranger polymerase	Bioline	#BIO21121
Q5 polymerase	New England Biolabs	#M0491S
Superscript III Reverse Transcriptase	Invitrogen	#18080093
normal goat serum (NGS)	Jackson ImmunoResearch	#005-000-121 RRID:AB_2336990
Vectashield®	Vector Laboratories	#H-1000
SQ22536	Merck	#568500
Triton X-100	Sigma-Aldrich	#1.08603
paraformaldehyde	Fluka	#76240
NaCl	Merck	#106404
KCl	Merck	#104936
$MgCl_2$	Merck	#105833
TES	Sigma-Aldrich	#T5691
sucrose	Sigma-Aldrich	#S9378
D-(+)-glucose	Sigma-Aldrich	#G7528
D-(+)-trehalose	Sigma-Aldrich	#T9531
$NaHCO_3$	Sigma-Aldrich	#S6297
NaH_2PO_4	Sigma-Aldrich	#71507
HEPES	Sigma-Aldrich	#54457
$CaCl_2$	Merck	#102382
Dulbecco's Modified Eagle medium (DMEM)	Sigma-Aldrich or Gibco	#D6429 or #11995065
Fetal Bovine Serum	Sigma-Aldrich or Gibco	#F7524 or #10500
Penicillin/Streptomycin	Sigma-Aldrich or Gibco	#P4333 or #15140122
Lipofectamine™ 2000	Invitrogen	#11668019
PBS tablets	Gibco	#18912014
2-mercaptoethanol	Sigma-Aldrich	#M6250

(*Continued on next page*)

Continued

REAGENT or RESOURCE	SOURCE	IDENTIFIER
SDS	Carl Roth	#2326
Tris	Carl Roth	#AE15
Tris/HCl	Carl Roth	#9090
EDTA	Carl Roth	#8040
DTT	Carl Roth	#6908
glycerol	Carl Roth	#3783
urea	Carl Roth	#7638
bromophenol blue	Sigma-Aldrich	#B8026
Tween 20	Serva	#37470
Intercept® (PBS) Blocking Buffer	LI-COR Biosciences	#927-70001
Protease Inhibitor Cocktail	Sigma-Aldrich	#P8340
M-PER™ Mammalian Protein Extraction Reagent	Thermo Scientific	#78503
4x Protein Sample Loading Buffer for Western Blots	LI-COR Biosciences	#928-40004
Critical commercial assays		
RNeasy RNA Isolation Kit	Qiagen	#74104
Pierce™ HA-Tag Magnetic IP/Co-IP Kit	Thermo Scientific	#88838
NucleoBond® Xtra Midi	Macherey & Nagel	#740410.50
Pierce™ BCA Protein Assay Kit	Thermo Scientific	#23227
ChromoTek RFP-Trap® Magnetic Agarose	Proteintech	#rtma
Experimental models: Cell lines		
HEK293T cells	German Collection of Microorganisms and Cell Cultures (DSMZ)	#ACC 635 RRID:CVCL_0063
Experimental models: Organisms/strains		
D. melanogaster: LAT1618, w^{1118}; $Cirl^{KO}$ {w^{+mC} = *pNH103 [RFP::Cirl$^{GPS\text{-}WT}$::2xV5::3xFlag w^{+}]}/CyoGFPw^{-};;* ($Cirl^{3x\text{-}tagged}$)		Co-expression of RFP::Cirl^{7TM}::3xFlag and RFP::Cirl^{1TM}::2xV5 isoforms from the endogenous locus. Related to Figure 2.
D. melanogaster: LAT1640, w^{1118}; $Cirl^{KO}${w^{+mC} = *pNH177 [RFP::Cirl$^{GPS/H>A}$::2xV5::3xFlag w^{+}]} attP^{Cirl}/CyoGFPw^{-};;* (Cirl$^{3x\text{-}tagged\text{-}GPS/H>A}$)		Co-expression of cleavage deficient RFP::Cirl$^{7TM\text{-}GPS/H>A}$::3xFlag and RFP::Cirl$^{1TM\text{-}GPS/H>A}$::2xV5 isoforms from the endogenous locus. Related to Figure 2.
D. melanogaster: LAT1642, w^{1118}; $Cirl^{KO}$ {w^{+mC} = *pNH217 [Cirl^{1TM} w^{-}]}attP^{Cirl}/CyoGFPw^{-};;* (Cirl$^{1TM\text{-}noV5}$)		Exclusive expression of untagged Cirl^{1TM} isoforms from the endogenous locus. Related to Figure S3.
D. melanogaster: LAT1619, w^{1118}; $Cirl^{KO}$ {w^{+mC} = *pNH191 [Cirl^{7TM}::2xV5 w^{-}]}attP^{Cirl}/CyoGFPw^{-};;* (Cirl^{7TM}::2xV5)		Exclusive expression of Cirl^{7TM}::2xV5 isoforms from the endogenous locus. Related to Figures 3A–3E and 4; Figure S2, S5.
D. melanogaster: LAT1541, w^{1118}; $Cirl^{KO}$ {w^{+mC} = *pNH190 [Cirl^{1TM}::2xV5 w^{-}]}attP^{Cirl}/CyoGFPw^{-};;* (Cirl^{1TM}::2xV5)		Exclusive expression of Cirl^{1TM}::2xV5 isoforms from the endogenous locus. Related to Figures 3A–3E and 4; Figure S2, S3, S5.
D. melanogaster: LAT1621, w^{1118}; $Cirl^{KO}$ {w^{+mC} = *pNH188 [RFP::Cirl^{1TM}::2xV5 w^{-}]}attP^{Cirl}/CyoGFPw^{-};;* (RFP::Cirl^{1TM}::2xV5)		Exclusive expression of RFP::Cirl^{1TM}::2xV5 isoforms from the endogenous locus. Related to Figure 3H.
D. melanogaster: LAT1511, w^{1118}; $Cirl^{KO}$ {w^{+mC} = *pNH275 [Cirl^{1TM}::mCD8-TM::6xV5 w^{-}]}attP^{Cirl}/CyoGFPw^{-};;* (Cirl^{1TM}::mCD8-TM:6xV5)		Expression of the ECR of Cirl fused to the single TM of mouse CD8. Expressed from the endogenous *Cirl* locus. Related to Figures 6A–6C.

(*Continued on next page*)

Continued

REAGENT or RESOURCE	SOURCE	IDENTIFIER
D. melanogaster: LAT1636, w^{1118}; $Cirl^{KO}${w^{+mC} = *pTL370 [dCirl]}attP*^{Cirl} *loxP;;* ($Cirl^{Rescue}$)	Scholz et al. (2015)	RRID:BDSC_602699
D. melanogaster: LAT1615, w^{1118}; $Cirl^{KO}$ *attPCirl loxP;;* ($Cirl^{KO}$)	Scholz et al. (2015)	RRID:BDSC_602706
D. melanogaster: LAT159, w^{1118}; $Cirl^{N\text{-}RFP}$;; (^{RFP}Cirl)	Scholz et al. (2017)	RRID:BDSC_93001
D. melanogaster: LAT1613, w^{1118}; $^{RFP}Cirl^{GPS\text{-}T>A}$;; ($^{RFP}Cirl^{GPS/T>A}$)	Scholz et al. (2017)	RRID:BDSC_602701
D. melanogaster: LAT112, w^{1118};; *P{iav-Gal4 w+}attP2;* (iav-GAL4)	Scholz et al. (2015)	
D. melanogaster: LAT1620, w^{1118}; $^{RFP}Cirl^{7TM-2xV5}$ w^{-};; ($^{RFP}Cirl^{7TM-2xV5}$)	Scholz et al. (2023)	RRID:BDSC_602683
D. melanogaster: GN393, *w*;UAS-dGαo, ZH-22A-3xP3-RFP/CyoGFPw;;* (UAS-dGαo)	Solis et al. (2017)	
D. melanogaster: w[1118]; PBac{y[+mDint2] w[+mC] = 20XUAS-IVS-jGCaMP7f} VK00005 (20xUAS-jGCamp7f)	Bloomington Stock Center	RRID:BDSC_79031
D. melanogaster: y[1] v[1]; P{y[+t7.7] v[+t1.8] = TRiP.JF01608}attP2 (UAS-GαiRNAi-1)	Bloomington Stock Center	RRID:BDSC_31133
D. melanogaster: y[1] sc[*] v[1] sev[21]; P{y[+t7.7] v[+t1.8] = TRiP.GL00328}attP2 (UAS-GαiRNAi-2)	Bloomington Stock Center	RRID:BDSC_35407
D. melanogaster: y[1] v[1]; P{y[+t7.7] v[+t1.8] = TRiP.JF02844}attP2 (UAS-GαoRNAi)	Bloomington Stock Center	RRID:BDSC_28010
Oligonucleotides		
Cloning $Cirl^{3x\text{-}tagged}$ vector nh_199F: tgattggcgatcgctgaaaaaacagataaacacaatttt	This paper	
Cloning $Cirl^{3x\text{-}tagged}$ vector nh_259R: aaggcctccaccaccaccacttatattgtaag	This paper	
Cloning $Cirl^{3x\text{-}tagged}$ vector nh_260F: cctggcaagcc catccccaaccccctgctgggcctggattccaccggcaag cccatccccaaccccctgctgggcctggattccacctgcgat	This paper	
Cloning $Cirl^{3x\text{-}tagged}$ vector nh_261R: cgcaggtgga atccaggcccagcaggggttggggatgggcttgccggtg gaatccaggcccagcaggggttggggatgggcttgccagg	This paper	
Cloning $Cirl^{3x\text{-}tagged,GPS/H>A}$ vector mn_38F: gcgtctgcagttgcaacgccctgacaaactttgcc	Scholz et al. (2017)	
Cloning $Cirl^{3x\text{-}tagged,GPS/H>A}$ vector mn_39R: ggcaaagtttgtcagggcgttgcaactgcagacgc	Scholz et al. (2017)	
RT-PCR $Cirl^{7TM}$ and $Cirl^{1TM}$ cDNA tl_5F: tcatcagggagcgcagcgtggtgca	This paper	
RT-PCR $Cirl^{7TM}$ cDNA tl_6R: atgctggtata gatcgaggtgcgcg	This paper	
RT-PCR $Cirl^{1TM}$ cDNA tl_329R: cgtgggtc tggtcgcgaatattgt	This paper	
RT-PCR Tubulin rk_16: gtgaattttccttgtcgcgtg	This paper	
RT-PCR Tubulin rk_17: ctccagtctcgctgaagaag	This paper	
Cloning HA::Cirl-E vector nh_588F: ctagtctagatgaactagagggccctattctatag	This paper	
Cloning HA::Cirl-E vector nh_589R: ctagaccggtcttagccagtggttccagataacat	This paper	
Cloning HA::Cirl-E vector nh_590F: ctagaccggtggaggcggtggcggc ggaaaaccca	This paper	

(*Continued on next page*)

Continued

REAGENT or RESOURCE	SOURCE	IDENTIFIER
Cloning HA::Cirl-E vector nh_591R: ctagtctagatcacgtcgaatcgagtccgagcag	This paper	
Cloning HA::Cirl-F/K$^{GPS/T>A}$, HA::Cirl-E$^{GPS/T>A}$ and Cirl-E$^{GPS/T>A}$::6xV5 vector mn_12F: cagttgcaaccacctggcaaactttgccatact	This paper	
Cloning HA::Cirl-F/K$^{GPS/T>A}$, HA::Cirl-E$^{GPS/T>A}$ and Cirl-E$^{GPS/T>A}$::6xV5 vector mn_13R: agtatggcaaagtttgccaggtggttgcaactg	This paper	
Cloning HA::Cirl-F/K vector jt_11F: tatcgccctgataacgctgaagctgttcaat ggggtctttgtgaagg	This paper	
Cloning HA::Cirl-F/K vector jt_15R: ctatagaatagggccctctagttcaccacc accaccacttatattgtaag	This paper	
Cloning HA::Cirl-F/K vector jt_14R: cagcttcagcgttatcagggcgata	This paper	
Cloning HA::Cirl-F/K vector jt_16F: tgaactagagggccctattctatagtgtcac	This paper	
Cloning HA::GPR126$^{7TM-GPS/T>A}$ and GPR126$^{1TM-GPS/T>A}$::6xV5 vector ab_10F: gtctgtgcagccacttcgctcactttggag	This paper	
Cloning HA::GPR126$^{7TM-GPS/T>A}$ and GPR126$^{1TM-GPS/T>A}$::6xV5 vector ab_11R: ctccaaagtgagcgaagtggctgcacagac	This paper	
Cloning Cirl-F/K$^{\Delta CTF}$::6xV5 vector ab_38R: ctagaccggtttcagctacgcaacccatc	This paper	
Cloning Cirl-F/K$^{\Delta CTF}$::6xV5 vector ab_39F: ctagaccggttttcccaagtcactcagcg	This paper	
Recombinant DNA		
Cirl::3x-tagged vector (pNH103)	This paper	
Cirl::3x-tagged$^{GPS/H>A}$ vector (pNH177)	This paper	
RFP::Cirl^{1TM}*::2xV5* vector (pNH188)	This paper	
Cirl^{1TM}*::2xV5* vector (pNH190)	This paper	
Cirl^{7TM}*::2xV5* vector (pNH191)	This paper	
Cirl^{1TM} *no tags* vector (pNH217)	Engineered by GenScript	
Cirl^{ECR}*-mCD8*^{TM} vector (pNH275)	Engineered by GenScript	
empty pcDNA3.1 vector (pSA25)	–	
empty pHLSec vector (pNH366)	Gift from Björn Kieslich	
HA::Cirl-E vector (pJT2)	This paper	
HA::Cirl-F/K vector (pJT9)	This paper	
HA::Cirl-F/K$^{GPS/T>A}$ vector (pJT11)	This paper	
Cirl-E::6xV5 vector (pNH354)	This paper	
Cirl-E$^{GPS/T>A}$*::6xV5* vector (pNH356)	This paper	
HA::Cirl-E$^{GPS/T>A}$ vector (pNH254)	This paper	
Cirl-F/K::6xV5 vector (pAB24)	This paper	
Cirl-F/K$^{GPS/T>A}$*::6xV5* vector (pAB25)	This paper	
Cirl-F/K$^{\Delta CTF}$*::6xV5* vector (pAB23)	This paper	
HA::GPR126^{7TM} vector (pNH364)	Engineered by GenScript	
GPR126^{1TM}*::6xV5* vector (pNH363)	Engineered by GenScript	
HA::GPR126$^{7TM-GPS/T>A}$ vector (pAB11)	This paper	
GPR126$^{1TM-GPS/T>A}$*::6xV5* vector (pAB9)	This paper	

(*Continued on next page*)

Continued

REAGENT or RESOURCE	SOURCE	IDENTIFIER
HA::P2Y12:Flag vector (pMIH57)	Gift from Torsten Schöneberg, transferred to pcDNA3.1	
Software and algorithms		
ImageJ/Fiji (NIH)	ImageJ.net	RRID:SCR_003070
GelAnalyzer v19.1	gelanalyzer.com	
Audacity v3.0.0	audacityteam.org	RRID:SCR_007198
HOKAWO v3.0	hamamatsu.com	
Omicron Control Center v3.6.18	Omicron-Laserage	
GraphPad Prism v6-9	Graphpad Software, Inc	RRID:SCR_002798
Leica Application Suite X (LAS X)	Leica Microsystems	RRID:SCR_013673
pClamp v10	Molecular Devices	RRID:SCR_011323
SigmaPlot v12	Systat Software	RRID:SCR_003210
BioRender	BioRender	
Tophat v2.0.14	https://ccb.jhu.edu/software/tophat/index.shtml	
Bowtie2 v2.1.0	https://sourceforge.net/projects/bowtie-bio/files/bowtie2/2.1.0/	
SAMtools v1.3.1	http://www.htslib.org/doc/1.3.1/samtools.html	
StringTie v1.3.3	https://ccb.jhu.edu/software/stringtie/	
Integrated Genome Viewer v2.3.91	https://igv.org	
Other		
Novex™ Tris-Glycine Mini Protein Gels, 8%	Invitrogen	#XP00080BOX
Novex™ Tris-Glycine Mini Protein Gels, 4–12%	Invitrogen	#XP04120BOX
Novex™ Tris-Glycine Mini Protein Gels, 4–20%	Invitrogen	#XP04200BOX
iBlot™ 2 Transfer Stacks, nitrocellulose	Invitrogen	#IB23001 and #IB23002
Sylgard	Dow Corning	#1673921
Minutien Pins	Fine Science Tools	#26002-10
Vannas-Tübingen Spring Scissors	Fine Science Tools	#15005-08
Dumont Forceps #4	Fine Science Tools	#11241-30
Dumont Forceps #5	Fine Science Tools	#11251-20
Dumont Forceps #55	Fine Science Tools	#11255-20
Borosilicate glass capillaries	Science products	#GB150-8P
Bath chamber (μ-Dish, 35 mm, low)	Ibidi	#80136
Leica S8 APO microscope	Leica Microsystems	
Leica DM6 FS microscope	Leica Microsystems	
Axopatch 200B amplifier	Molecular Devices	
Axon Digidata 1550B analog-digital converter	Molecular Devices	
DMZ Universal electrode puller	Zeitz-Instruments	
Piezo element	Physik Instrumente	#P-840.30
Piezo amplifier	Physik Instrumente	#E-663.00
Micromanipulator system	Sutter Instrument Company	#MPC-385
Micromanipulator	Narishige group	#NMN-25
LedHUB light source	Omicron-Laserage	
ORCA-flash4.0 sCMOS camera	Hamamatsu	C13440
SL-100 SPL meter	VOLTCRAFT	
X210 loud speaker	Logitech	
Ultraturrax disperser T10 basic	IKA-Werke	#0003737000
Ultraturrax dispersing element S 10 *N* - 5 G	IKA-Werke	#0003304000

(*Continued on next page*)

Continued

REAGENT or RESOURCE	SOURCE	IDENTIFIER
Actuator to gate loud speakers	Self-made	
Leica TCS SP8 confocal microscope	Leica Microsystems	
Odyssey® Fc 2800	LI-COR Biosciences	

EXPERIMENTAL MODEL AND STUDY PARTICIPANT DETAILS

Drosophila stock and culture

All *Drosophila* strains (key resources table) were reared in food containing: 60% water, 3.4% agar, 9% yeast, 5% soy flour, 40% corn flour, 0.7% nipagin, 9% treacle and 0.52% propionic acid. *Drosophila* were kept at 25°C and a 12h light/dark cycle. Transgenic flies used, were either generated in this study or obtained from Bloomington Drosophila Stock Center. Third-instar larvae were synchronized and staged by selecting the largest animals still crawling in the food.

HEK293T cells (RRID:CVCL_0063) were cultivated in Dulbecco's Modified Eagle Medium supplemented with 10% (v/v) fetal bovine serum and 1% penicillin/streptomycin at 37°C and a 5% CO_2 humidified atmosphere.

METHOD DETAILS

Molecular cloning

Cirl cDNAs were N-terminally complemented with a mammalian Kozak sequence (gccacc), followed by the start codon, signal peptide (SP) of mammalian ADGRG1/GPR56, an HA-tag (*HA::Cirl-X)* and are contained in the *CMV* promoter-containing pcDNA3.1 backbone. *Cirl^{1TM}* constructs used for immunoprecipitation experiments contained six V5-tags at their C-termini, but no HA-tag (Cirl^{1TM}::6xV5). Plasmid amplification was done via transformation in *E. coli* (XL1-Blue, DH5α or EPI400) and DNA isolation via Midiprep (NucleoBond Xtra Midi, Macherey & Nagel). The Ranger (Bioline, #BIO21121) or Q5 (New England Biolabs, #M0491S) high-fidelity proof-reading DNA polymerases were utilized for all PCR-based cloning steps. Initial insert verification was done by restriction fragment analyses. To ensure absence of errors each PCR-amplified region was sequenced.

Cirl$^{3x\text{-}tagged}$ *vector (pNH103)*

Primers *nh_199F/259R* were used to amplify a 4.9-kbp fragment from *pMN21* (genomic 1.9-kbp *Cirl* subclone) and to introduce *Sgf*I and *Stu*I restriction sites at the 3′ and 5′ end, respectively.

2xV5-tag was generated using *nh_260F/261R*, which contained *Sgf*I and *Stu*I sites for subsequent ligation with 4.9-kbp fragment (resultant subclone *pNH101*). *Cirl::2xV5* fragment was transplanted from *pNH101* into *pMN24* (genomic *RFP::Cirl::3xFlag* construct) via *Pac*I and *Spe*I restriction sites, resulting in *pNH103*.

Cirl$^{3x\text{-}tagged\text{-}GPS/H>A}$ *vector (pNH177)*

Primers *mn_38F/39R*[24] were used to substitute the histidine codon of the canonical GPS sequence for an alanine codon through site-directed mutagenesis of *pNH101*, which resulted in *pNH176*. *Pac*I/*Spe*I fragment of *pNH176* was cloned into *pNH103* resulting in *pNH177*.

RFP::Cirl^{1TM}::2xV5 *vector (pNH188)*

Genomic sequence encoding *RFP::Cirl^{1TM}::2xV5* (~3.9 kbp) in pMK backbone was synthesized by ThermoFisher/GeneArt (resulting construct *pNH186*). A 3.9-kbp fragment was cloned into the expression vector using *Mlu*I and *BstB*I sites to generate *pNH188*.

Cirl^{1TM}::2xV5 *vector (pNH190)*

*Age*I-based removal of mRFP sequence and subsequent re-circularization of *pNH188* resulted in *pNH190*.

Cirl^{7TM}::2xV5 *vector (pNH191)*

*Age*I-based removal of mRFP sequence and subsequent re-circularization of *pNH189* resulted in *pNH191*.

Cirl^{1TM} no tags *vector (pNH217)*

Engineered by GenScript.

Cirl^{ECR}-mCD8 *vector (pNH275)*

Engineered by GenScript.

Cirl$^{1TM\text{-}GPS/H>A}$::2xV5 (pNH310)

Engineered by GenScript.

Cirl$^{7TM\text{-}GPS/H>A}$::2xV5 (pNH311)

Engineered by GenScript.

PhiC31-mediated integration of transgenes

Plasmids containing w^+ and an *attB* site were injected into *phiC31[3xP3-RFP-3xP3-GFP-vas-PhiC31]; Cirl^{KO} attP-loxP;;* embryos (done by BestGene).[10] w^+ served as the selection marker to identify recombinants and was subsequently removed by Cre-mediated excision (done by BestGene). Precise transgene insertion and removal of w^+ *cassette* were validated by PCR genotyping.

RT-PCR

Total RNA was isolated from larvae and adult w^{1118} animals using RNeasy RNA Isolation Kit (Qiagen) and was directly used for reverse transcription using Superscript III Reverse Transcriptase according to manufacturer's protocol (Invitrogen). PCR amplification from cDNA libraries was carried out using primers tl_5F, tl_6R, tl_392R, rk_16, rk_17.

RNA-sequencing analyses

RNA-sequencing datasets that document the transcriptome at 30 distinct developmental stages of the *y1; cn bw1 sp1 Drosophila melanogaster* strain[23] from NCBI Sequence Read Archive (SRA, https://www.ncbi.nlm.nih.gov/sra)[71] were chosen to analyze and quantify *Cirl* transcripts during ontogenesis. Reads were mapped to the reference *Drosophila melanogaster* genome (July 2014, BDGP6 (GCA_000001215.4)) with Ensembl 88 annotations using Tophat 2.0.14.,[72] which aligns reads using Bowtie2 (version 2.1.0). Reads, which did not map uniquely to a genome position were excluded. After indexing with SAMtools (version 1.3.1),[73] the mapped reads were assembled to transcripts and quantified by StringTie (version 1.3.3).[74,75] For Tophat, we used the 'default' parameters, which are commonly used in most studies. StringTie parameters 'read coverage' (-c), 'transcript length' (-m) and 'bases on both sides of a junction a spliced read has to cover' (-a) were set to minimal values in order to avoid missing transcripts and generating a bias. The parameter 'fraction of most abundant transcript at one locus' (-f) was lowered from default (0.01) to 0 since correction for artifacts and incompletely processed mRNA with a 1% cutoff was performed after the comparative analysis. For all other StringTie parameters, default values were used. Assembled transcripts were inspected with the Integrated Genome Viewer (Broad Institute) (version 2.3.91),[76,77] and samples showing a visible 3′ bias due to oligo-dT/poly-A primer selection were not included.

Cell culture

HEK293T cells (RRID:CVCL_0063) were cultivated in Dulbecco's Modified Eagle Medium (DMEM; Sigma-Aldrich, #D6429 or Gibco, #11995065) supplemented with 10% (v/v) fetal bovine serum (Sigma-Aldrich, #F7524 or Gibco, #10500) and 1% penicillin/streptomycin (Sigma-Aldrich, #P4333 or Gibco, #15140122) at 37°C and a 5% CO_2 humidified atmosphere.

HEK293T cells were split into 6-well cell culture plates ($4x10^5$ cells/well) for co-immunoprecipitation analysis. After 24 h cells were transiently transfected with 2.5 μg plasmid DNA per well using Lipofectamine 2000 (Invitrogen, #11668019) according to manufacturer's recommendations. Cells were incubated 48 h post transfection in a 5% CO_2 humidified atmosphere at 37°C. After 24 h, cell culture medium was exchanged against 2 mL DMEM.

Immunofluorescence and imaging

Third instar *Drosophila* larvae were dissected in ice-cold HL-3 (hemolymph-like solution),[78] fixed for 10 min using ice-cold 4% paraformaldehyde in 0.1 M phosphate buffered saline (PBS) and blocked overnight in PBT (PBS with 1% Triton X-100, Sigma-Aldrich), containing 5% normal goat serum (NGS, Jackson ImmunoResearch). Primary antibody incubation was done at 4°C overnight. The next day, secondary antibody incubation was done for 24 h, at 4°C. Each antibody incubation step was followed by two short and three 20 min washing steps (PBS with 1% Triton X-100). Samples were stored in Vectashield (Vector Laboratories) overnight at 4°C before mounting. Confocal imaging was performed with a Leica SP8 confocal system. To ascertain comparability between different genotypes, larvae were imaged in one session and image acquisition of genotypes alternated. Image analysis was done using ImageJ (NIH). Antibodies and dyes were used at following dilutions: rabbit-*anti*-dsRed (1:500, Takara, #632496; RRID:AB_10013483), anti-HRP conjugated with Alexa Fluor 488 (1:250; Jackson ImmunoResearch, #123-545-021, RRID: 2338965), Cy5-conjugated goat-*anti*-rabbit (1:250; Jackson ImmunoResearch, #111-175-144, RRID: AB_2338013).

Protein isolation

HEK293T cells

Cells were lysed using 200 μL M-PER buffer (ThermoFisher, #78503) supplemented with protease inhibitor (1:1000, Sigma-Aldrich, #P8340). After addition of lysis buffer, cells were detached from the culture dish bottom using a cell scraper and incubated on ice for 5 min. Transferred samples were then centrifuged for 5 min at 14,000 rpm (4°C) and a sample of the supernatant diluted 4:1 with 4x sample buffer (Licor, #928–40004) containing 10% (v/v) 2-mercaptoethanol. Total protein concentration was determined using the Pierce BCA Protein Assay Kit (ThermoFisher, #23227). Note that within a co-immunoprecipitation experiment, the same amount of total protein was used.

Fly heads

Fly heads (25/genotype) were severed using fine scissors (Fine Science Tools, #15005-08), collected in 0.5 mL Eppendorf tubes and immediately frozen in liquid nitrogen. Subsequently, the heads were homogenized in 2% SDS supplemented with a protease inhibitor cocktail (1:1000; Sigma-Aldrich) using a glass rod (4°C). Next, Triton X-100 was added (final concentration 1%) to the samples, which were then centrifuged for 15 min (14,000 rpm) at 4°C. The supernatant was collected in fresh, pre-cooled tubes and centrifuged twice again for 30 min at 14,000 rpm and 4°C. Finally, the supernatant was supplemented with SDS-based sample buffer (LI-COR) and 2-mercaptoethanol (Merck).

Pupae

One-to two-day-old pupae (~0.6 g/genotype) were collected, immediately frozen in liquid nitrogen and homogenized in a pre-cooled mortar using a pestle. The resulting protein powder was transferred into a pre-cooled tube and supplemented with homogenization

buffer (50 mM Tris/HCl, 150 mM NaCl, 1% Triton X-100, Protease Inhibitor 1:1000, 1 mM DTT, pH 7.4). Samples were further homogenized using an Ultra-Turrax (4 × 15 s; IKA T10 Basic). Next, samples were centrifuged at 4,000 x g for 30 min, again at 14,000 x g for 30 min and finally at 25,000 x g for 60 min. The samples were kept at 4°C throughout the procedure. Finally, the supernatant was supplemented with 5x Laemmli buffer (250 mM Tris, 12.5 mM EDTA, 10% SDS, 25% glycerol, 8 M urea, 0.025% bromophenol blue, 200 mM DTT) or sample buffer (LI-COR) supplemented with 2-mercaptoethanol.

Immunoblots

Protein samples were electrophoretically separated using 8%, 4–12% or 4–20% Tris-glycine gradient gels and blotted (protein from fly heads: 15 V, 7 min; protein from HEK293T and fly pupae: 15 V, 6 min) onto nitrocellulose membrane (0.2 μm pore diameter, iBlot Transfer stack, ThermoFisher, #IB23001/#IB23002) using the iBlot2 (Invitrogen). The membrane was blocked for 1h using Odyssey Blocking buffer (LI-COR, #927–40000) diluted 1:2 with PBS. Blots were probed with primary antisera at indicated concentrations overnight at 4°C: rabbit-α-RFP (1:1000, Antibodies-Online, RRID:AB_10781500), mouse-α-V5 (1:1000, Invitrogen, RRID:AB_2556564), rabbit-α-HA (1:1000, C29F4, Cell signaling technology; RRID:AB_1549585), rabbit-α-Tubulinα (1:5000, Santa Cruz antibodies, #12462-R), mouse-α-Tubulinβ (1:2000, Developmental Studies Hybridoma Bank e7, RRID: AB_528499).

After rinsing twice and 3 × 5 min washing steps using 0.1% Tween-20-containing PBS, membranes were incubated with secondary antibodies from LI-COR (1:15,000): IRDye 680RD goat-α-mouse (RRID: AB_10956588), IRDye 680RD goat-α-rabbit (RRID: AB_10956166), 800CW goat-α-mouse (RRID: AB_621842), 800CW goat-α-rabbit (RRID: AB_621843) for 1 h, at RT and again rinsed twice and washed 3 × 5 min. Western blots were imaged with an OdysseyFc 2800 (LI-COR). The molecular weight of Western Blot bands was determined using the GelAnalyzer 19.1 software (gelanalyzer.com, by Istvan Lazar Jr., PhD and Istvan Lazar Sr., PhD, CSc.).

IP from pupae-derived proteins

Immunoprecipitation of *Drosophila* pupal lysates was performed using ChromoTek RFP Trap Magnetic Agarose beads (Proteintech, #rtma) according to manufacturer's recommendations. Protein was eluted by resuspension of beads in 1x Laemmli buffer or 1x sample buffer (LI-COR) and cooking at 95°C for 10 min.

Co-IP from HEK293T cell-derived proteins

Co-immunoprecipitation was performed using the HA-Tag Magnetic IP/Co-IP Kit (Pierce, ThermoFisher, #88838). The manufacturer's Manual IP/Co-IP protocol and the Elution Protocol using sample buffer (LI-COR) were applied.

Protein quantification

Western Blot images were analyzed according to[79] using the Gel Analyzer feature in ImageJ/Fiji (NIH). Each lane in the image of the WB or co-IP membrane was selected and added to the Gel Analyzer to obtain profile plots of each lane. Each band is represented as an intensity profile, the area under which was used for quantification. For the analyses of Western blots of co-IP experiments, the area under the intensity profile of the heavy chain of the magnetic bead HA-antibody was used to normalize signals of the bands in the same lane. The percentages of the total peak area were used to calculate the relative densities for each sample. This procedure was repeated for each replicate individually.

Ca^{2+} imaging

To compare the effects of different *Cirl* mutations on lch5 function, the genetically encoded Ca^{2+} indicator jGCaMP7f[28] was expressed under *UAS* control, using the *iav-gal4* driver[10] in homozygous $Cirl^{Rescue}$, $Cirl^{KO}$, $Cirl^{1TM}$, $Cirl^{7TM}$ and $Cirl^{1TM+7TM}$ backgrounds. Non-wandering male third-instar larvae were pinned to a Sylgard pad in ice-cold, Ca^{2+}-free HL-solution[10,80] and cut open along the dorsal midline. The body muscle wall was gently stretched to the sides and pinned to the pad with minutien pins (#26002-10, Fine Science Tools). Innards and the CNS were gently removed. The Sylgard pad was transferred to the imaging chamber, filled with 2 mM $CaCl_2$-containing HL-solution. To stimulate the lch5 mechanically, a 900 Hz tone (sine wave) of different intensities (75–90 dB SPL, starting with 75) was applied via a small suspended computer loudspeaker. Lch5 activity pattern was unchanged even when stimulus direction was moved 180° from its initial position (data not shown). The sound frequency was controlled by Audacity software (V3.0.0, audacityteam.org). Stimulation intensity was verified by measuring sound pressure levels prior to every experiment. At small stimulation intensities, several measurements were averaged to increase the signal to noise ratio: 75 dB, 10 measurements; 80 dB, 5 measurements. Fluorescence imaging of the jGCaMP7f signal was performed on a DM 6FS (Leica) upright microscope equipped with a 40x, 0.8 N.A. dip-in objective and a GFP filter cube: excitation, 450–490 nm; dichroic 495 nm; emission, 500–550 nm. After pre-bleaching samples for 90 s to reduce bleaching rates during the experiment, samples were illuminated by blue LED light of the same intensity (LedHUB equipped with a LedH.465.4600, Omicron Laserage). jGCaMP7f fluorescence signals were video-recorded with a Hamamatsu Orca flash 4.0, V3 sCMOS camera at a 25-Hz frame rate and a 163 × 163 nm pixel size. Ten larvae of each genotype were measured. Videos were digitized and stored using the HOKAWO 3.0 software (Hamamatsu) and imported to Fiji ImageJ (NIH). A round, five-pixel diameter region of interest (ROI) was placed at the distal end of lch5 dendrites. The time course of the mean fluorescence intensity (F) in the ROI was exported to GraphPad Prism 6. $\Delta F/F_0$ was determined by calculating F_0, i.e., the mean intensity during the 0.36 s period before stimulation and normalizing ΔF (i.e., $F - F_0$) to F_0. To quantitatively compare

Ca^{2+} signals between genotypes, the $\Delta F/F_0$ averages of the Ca^{2+} signal plateaus (second half of the stimulation period) were calculated. Videos, in which any movement was detected, were discarded.

Electrophysiology

To compare the effects of different *Cirl* alleles on lch5 function, non-wandering male third-instar larvae were dissected as described in 'Ca^{2+} imaging'. After the innards and the CNS were removed, longitudinal muscles of the third, right abdominal hemisegment were cut cautiously. The lch5 nerve bundle was cut near the ventral, anterior end of muscle 21. The muscles 21, 22 and 23 were carefully cut and removed. The Sylgard pad was transferred to the recording chamber, filled with 2 mM $CaCl_2$-containing HL-solution.[81] Micropipettes with 6–10 μm diameters were fabricated using the electrode puller. To perform action current (ACurr) recordings, the pipette, which harbored the Ag/AgCl electrode, was filled with the bath solution. The lch5 nerve bundle was sucked into the pipette, and its opening was moved close to the soma of the neurons. Electrical activity was measured in voltage-clamp mode at 0 V using the Axopatch 200B amplifier. The measured current was low-pass Bessel filtered at 1 kHz and digitized at 10 kHz with the analog-digital converter and Clampex 10.2 Software. To stimulate the lch5 neurons, cap cells were perpendicularly hooked with a miniature stimulation hook made from minutien pins. The hook was glued to a glass micropipette, which in turn was attached to a piezo element. Pulls of 0.03, 0.1, 0.3, 1, and 3 μm were administered by applying negative voltage jumps to the piezo using the E663 amplifier, thus deflecting the lch5 to the side. Pull lengths of 3 μm and 1 μm were confirmed optically. The voltages for the 0.3, 0.1, and 0.03 μm had to be extrapolated from the voltages of longer pulls. Although the setup was thoroughly mechanically uncoupled, the hook most probably moved relatively to the organ by a much larger distance than the shortest pull length. Therefore, a reliable 30 nm pull seems unrealistic at first glance. However, since the piezo movement is very fast, its stability was measured as ±10 nm, and the organ reacts to stimulation in a differential manner, a meaningful reaction to the 30 nm pull could be easily detected. Each pull length, starting with 0.03 μm, was applied three times for 500 ms with a 1-s break between the pulls. After a 7 s pause, the next pull length was applied three times. ACurr during the first 50 ms were manually counted, as it is the time frame, when frequency increase mainly takes place. The ACurr frequency was calculated and evaluated in SigmaPlot 12. The mean of the three values of the same pull length was calculated to give $N = 1$. Ten measurements in ten different animals per genotype were performed. Treatment with the adenylyl cyclase inhibitor was carried out by adding 100 μM SQ22536 to the bath solution followed by 10 min incubation before starting the electrophysiological measurement. For sham treatment, the adenylyl cyclase inhibitor was replaced with water.

QUANTIFICATION AND STATISTICAL ANALYSIS

If not stated otherwise, data are reported as mean ± SEM, n indicates the sample size, which was not predetermined by statistical methods. Data were analyzed with Prism v6 – 9 (GraphPad). Data distribution was initially tested for normality with a Shapiro-Wilk test. Two set comparisons were done using two-tailed Student's t-tests, unless data was non-normally distributed. In this case, groups were compared by non-parametric tests (Mann-Whitney test for unpaired and Wilcoxon-Signed Rank test for paired comparisons).

Multiple comparison analyses (groups compared to every other group) were conducted with an ordinary One-way ANOVA followed by Tukey's multiple comparison test (for normally distributed samples), or a Kruskal-Wallis test followed by Dunn's multiple comparisons test (for non-normally distributed samples). Multiple comparisons (group compared to a single control) were done using One-way ANOVA followed by Dunnett's (for normally distributed samples) or the Kruskal-Wallis test followed by Dunn's multiple comparisons test (for non-normally distributed samples). Data presented in figures were statistically assessed as indicated:

Figures 4G–4I: One-way ANOVA, Tukey's test.
Figures 5D and 5G: One-way ANOVA, Tukey's test.
Figure 5J: One-way ANOVA, Dunnett's.
Figures 6B–6D: One-way ANOVA, Tukey's test.
Figure 6E: unpaired Student's t-test.
Figures 6F–6H: One-way ANOVA, Tukey's test.
Figure S2D,E: Kruskal-Wallis test, Dunn's test.
Figure S3: One-way ANOVA, Tukey's test.
Figure S5B-E top: Kruskal-Wallis test, Dunn's test.
Figure S5B-E bottom: One-way ANOVA, Dunnett's test.